CRASH Simulation of Rayleigh-Taylor, Richtmyer-Meshkov, and Magnetic Rayleigh-Taylor Instability

by

Jason Chuan-Chih Chou

A dissertation submitted in partial fulfillment
of the requirements for the degree of
Doctor of Philosophy
(Applied Physics)
in The University of Michigan
2013

Doctoral Committee:

      Professor R. Paul Drake, Chair
      Research Scientist Bruce A. Frywell
      Assistant Professor Eric Johnsen
      Research Scientist Carolyn Kuranz
      Professor Kenneth G. Powell

To all self-aware beings, who I pledge my allegiance to

ACKNOWLEDGEMENTS

TABLE OF CONTENTS

LIST OF FIGURES

LIST OF TABLES

LIST OF ABBREVIATIONS

AMR adaptive mesh refinement

BATS-R-US Block-Adaptive Tree Solarwind Roe Upwind Scheme

CFD Computational Fluid Dynamics

CFL Courant-Friedrichs-Lewy

CRF carbonized resorcinol formaldehyde

CRASH Center for Radiative Shock Hydrodynamics

EOS Equation of State

KHI Kelvin-Helmholtz instability

MHD magnetohydrodynamics

PLIF planar laser-induced fluorescence

PSAAP Predictive Science Academic Alliance Program

RMI Richtmyer-Meshkov Instability

RTI Rayleigh-Taylor Instability

SNRT Supernova Rayleigh-Taylor

ABSTRACT

CRASH Simulation of Rayleigh-Taylor, Richtmyer-Meshkov, and Magnetic
Rayleigh-Taylor Instability

by

Jason Chuan-Chih Chou

Chair: R. Paul Drake

The research discussed in this thesis was motivated by the supernova Rayleigh-Taylor
(SNRT) experiments conducted in 2009. Originally designed as laboratory astro-
physics experiments relevant to the Rayleigh-Taylor Instability (RTI) at the He-H
interface during supernova explosion, these experiments exhibited unusual late-time
morphology development, characterized by the lack of mushroom caps and uniform
width of the spikes. In response, a "Magnetic Straitjacket" hypothesis was proposed to
explain the discrepancy, based on the Biermann Battery mechanism. In order to test
this hypothesis, we used the Center for Radiative Shock Hydrodynamics (CRASH)
code developed for a sufficiently similar problem and with the necessary capabilities.
We validated this alternative usage of the CRASH code with simulations of pure
hydrodynamic RTI and RMI and identified the suitable combinations of numerical
schemes and parameters. For the RTI, we compared the results of simulations to the
analytical solution for the early time behavior, examined the late-time morphology,
and tested the low-resolution limit for the RTI simulations using CRASH. For the
RMI, we modeled Collins and Jacobs' experiment and compared the results of CRASH

simulations to the experimental observations as well as to the simulation results of several other code packages. Finally, we modeled the original SNRT experiments with magnetohydrodynamics (MHD) and Biermann battery effect. Unfortunately, the results were inconclusive due to insufficiently resolved simulations, limited by the explicit time integration of the magnetic diffusion. Furthermore, pilot runs with higher resolution indicated that simulations that fully resolve the gradients necessary to calculate the Biermann battery effect may be susceptible to the development of extraneous small-wavelength instabilities. Developments of implicit time integration of the magnetic diffusion and possibly new numerical schemes are therefore necessary for further progress, either with the CRASH code or other Eulerian code packages.

CHAPTER I

Introduction

1.1 CFD and Laboratory Astrophysics

Riding on the exponential scaling of Moore's Law, computation has risen rapidly to prominence in scientific inquiry and is now widely referred to as the "third leg" of science, in addition to theory and experiment. Computer simulation is now used to explore virtually every time and spatial scale humans have contemplated, from lattice quantum chromodynamics (QCD) [13], protein folding and dynamics [24], cellular metabolism [14], Antarctic ice sheet evolution [44], global climate system [51], all the way to the formation of the large-scale structure of the Universe [53].

Among the diverse applications of computation in science, Computational Fluid Dynamics (CFD) is one of the oldest disciplines. In fact, the first attempt of CFD predates the invention of modern programmable computer by decades and was carried out by human computers [46]. The Courant-Friedrichs-Lewy (CFL) condition was published in 1928 [8] and 3-dimensional calculations were first attempted in the 1960s, but the high-resolution methods with flux limiters we use today were only made possible in the 1970s by pioneers like Bram van Leer [3, 58, 30].

In general, systems considered by CFD are described by the Navier-Stokes equations. For systems in which viscosity is negligible, however, the conservation equations

can be simplified to the Euler equations:

$$\frac{\partial \rho}{\partial t} + \nabla \cdot (\rho \mathbf{u}) = 0 \tag{1.1a}$$

$$\rho \left(\frac{\partial}{\partial t} + \mathbf{u} \cdot \nabla \right) \mathbf{u} + \nabla p = \mathbf{0} \tag{1.1b}$$

$$\frac{\partial E}{\partial t} + \nabla \cdot (\mathbf{u}(E + p)) = 0, \tag{1.1c}$$

where ρ is the density, p is the pressure, $\mathbf{u}$ is the velocity vector, and $E = \rho e + \frac{1}{2}\rho u^2$ is the total energy density per unit volume of the fluid. For completeness, we also need an Equation of State (EOS) of the fluid in question to relate internal energy per unit mass e to pressure: for example, $p = \rho(\gamma - 1)e$ for ideal gas with adiabatic index γ. Regardless of the particular EOS, however, the behavior of systems described by the Euler equations does not depend on the time and spatial scale in the sense that they are invariant under the transformation $\mathbf{r} \rightarrow a\mathbf{r}'$, $\rho \rightarrow b\rho'$, $p \rightarrow cp'$, with $\mathbf{u} \rightarrow \sqrt{\frac{c}{b}}\mathbf{u}'$ and $t \rightarrow a\sqrt{\frac{b}{c}}t'$ as the consequences. Experimentally, this means that we can study any systems in the laboratory with appropriate scaling, as long as they are well-described by the Euler equations. The same cannot be said when the viscosity necessitates the full description by the Navier-Stokes equations, or when the magnetic field requires the full magnetohydrodynamics (MHD) treatment [48].

Situations where such Euler similarity applies represent one of the best case scenarios for laboratory astrophysics, the discipline that studies astrophysical conditions and dynamics by replicating them in the laboratory. Studies of the former demand access to the same physical parameters found in astrophysical systems and include examples such as measurement of the EOS of hydrogen/deuterium under the extreme pressure of the interiors of Jupiter and Saturn [49], the opacity of the plasma in the interior of the sun [1], and the rate of nuclear reaction in the main-sequence stars [7]. Studies of the dynamics, on the other hand, require careful scaling of parame-

ters necessitated by the size of laboratory systems and include examples such as an intergalactic plasma jet [16], layer mixing during a supernova explosion [11], and the interactions between the resulting shock and interstellar clouds [29]. The experiments relevant to this thesis replicate the mixing between the hydrogen layer and helium layer during the supernova explosion of SN1987A, mainly due to Rayleigh-Taylor Instability (RTI).

1.2 Hydrodynamic Instabilities and Supernovae

1.2.1 Rayleigh-Taylor Instability

RTI is an ubiquitous phenomenon, playing important roles both in our daily experience and under extreme conditions. The most intuitive, if somewhat restrictive condition for RTI to occur is when two layers of fluid are set on top of each other under constant gravity, with the heavy fluid with higher density ρ_2 on the top and light fluid with density ρ_1 on the bottom. Notice that even though we know intuitively that such arrangement is implausible, nothing in the Euler equations precludes it: as long as the lighter fluid provides sufficient hydraulic pressure, the heavy fluid can be supported on the top. The problem rises when there is some perturbation in the system, say the slightest variation in thickness of the heavy fluid. The light fluid couldn't compensate the additional weight of the the thicker part of the heavy fluid, so it drops and grows even thicker. As the result, the arrangement quickly collapses with positive feedback (Figure 1.1).

Since the effects of gravity and acceleration in the opposite direction are indistinguishable, a more general condition for RTI is when light fluid is accelerated into heavy fluid: for example, when the density gradient and pressure gradient are opposite to each other. This condition is more applicable in systems under extreme pressure and temperature, where the effect of gravity is less relevant. A supernova

explosion, following gravitational collapse, is the most drastic example.

Core-collapse supernovae like SN1987A are produced by sufficiently massive stars at their end of life. As the star burns through its lighter elements in nuclear reactions, heavier elements accumulate in layers closer to the core, while the remaining hydrogen and helium form its outermost layers. This process cannot continue indefinitely, however: the nucleus of iron is stable and cannot undergo any exothermic nuclear reaction. Consequently, iron accumulates at the core, which does not provide energy and pressure to counterbalance gravity any more. The core ultimately collapses upon itself, and the rebound creates a powerful blast wave which propagates outwards — an explosion in common language. As its defining feature, the shock front of the blast wave is followed by a self-similar tail of decreasing pressure. An exploding supernova therefore, with density gradient pointing inwards and pressure gradient pointing outwards, satisfies the condition for RTI (Figure 1.2). Motivated by observations of the SN1987A remnant (Figure 1.3), the case for the role of RTI during supernovae is further supported by computer simulation (Figure 1.4).

While RTI is mainly responsible for the initial layer mixing of supernovae, it is not the only hydrodynamic instability at play. In particular, it's preceded by Richtmyer-Meshkov Instability (RMI), and followed by Kelvin-Helmholtz instability (KHI).

1.2.2 Richtmyer-Meshkov Instability

RMI occurs when a shockwave is refracted by an interface between two materials (Figure 1.5). Since such an event applies an impulse, i.e. sudden acceleration, to the interface, RMI can be intuitively considered as a variant of RTI, with a Dirac delta function as the acceleration term. This "impulsive model", proposed by Richtmyer himself [47], turned out to be a very crude approximation and more recently refined with nonlinear perturbation theory [60]. At the same time, the case with small perturbations in density, pressure and velocity has been solved with linearized Euler
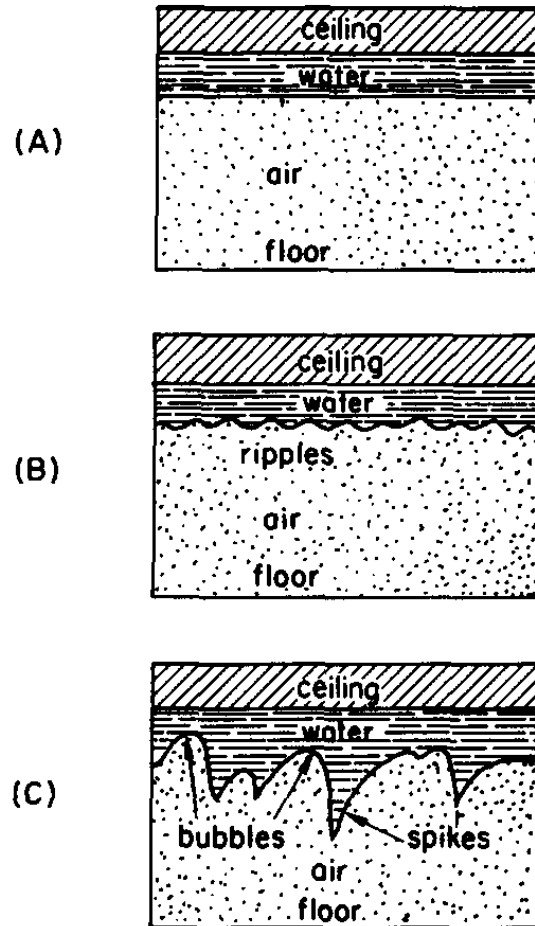
Figure 1.1: Illustration of RTI. The atmospheric pressure is more than enough to support a 1m layer of water on the ceiling (A). But as long as the water layer is not perfectly uniform and still (B), the thick part will grow thicker and drop, while the air will float up against the part of the water layer that is getting thinner and thinner (C). The extension of the heavy fluid is called "spike" and the extension of the light fluid is called "bubble". Figure from [50].
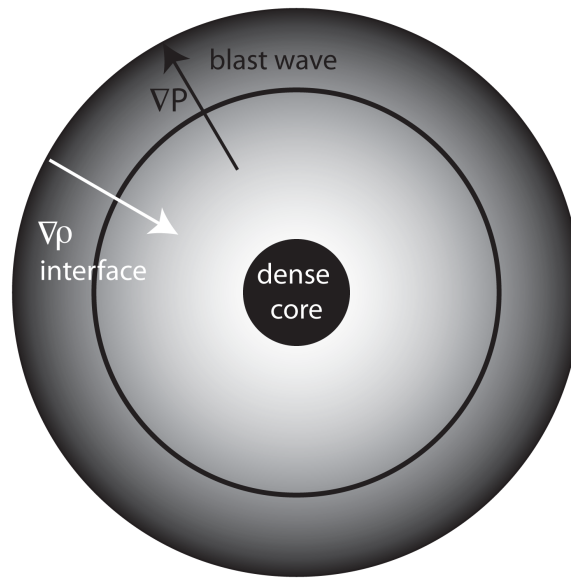
Figure 1.2: Diagram of an exploding supernova. The inner layers are denser and composed of elements with higher atomic number, and the shock front of the blast wave is followed by a self-similar, subsonic tail with decreasing pressure. The condition for RTI is therefore satisfied at the boundary between layers. Figure from Carolyn C. Kuranz's thesis, [36].
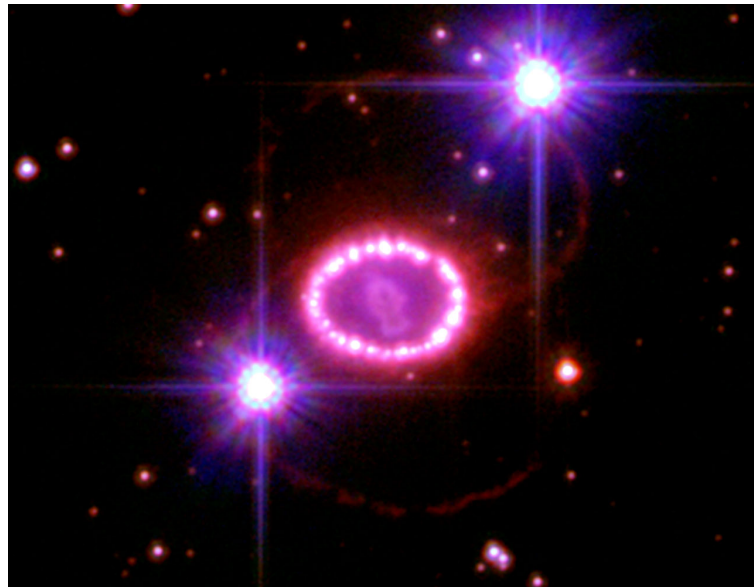
Figure 1.3: Remnant of SN1987A. Nicknamed "Cosmic Pearls", the anisotropy is clearly visible and explained by hydrodynamic instabilities. Photo taken by Advanced Camera for Surveys on Hubble Telescope in December 2006.
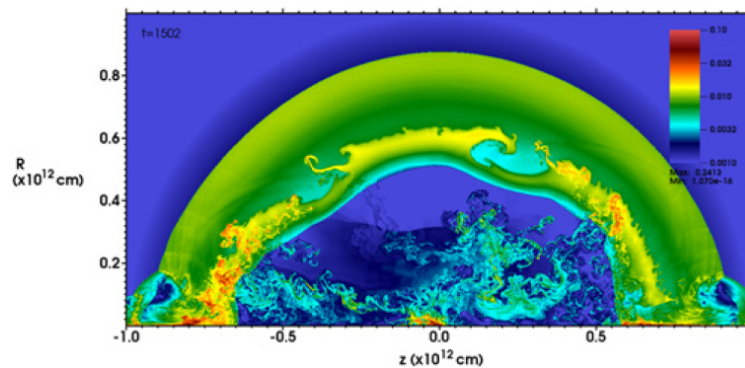
Figure 1.4: 2D simulation result of exploding supernova from [20], showing the density distribution $t = 1500$s after core bounce. The hydrogen bubbles are visible at the outermost interface.
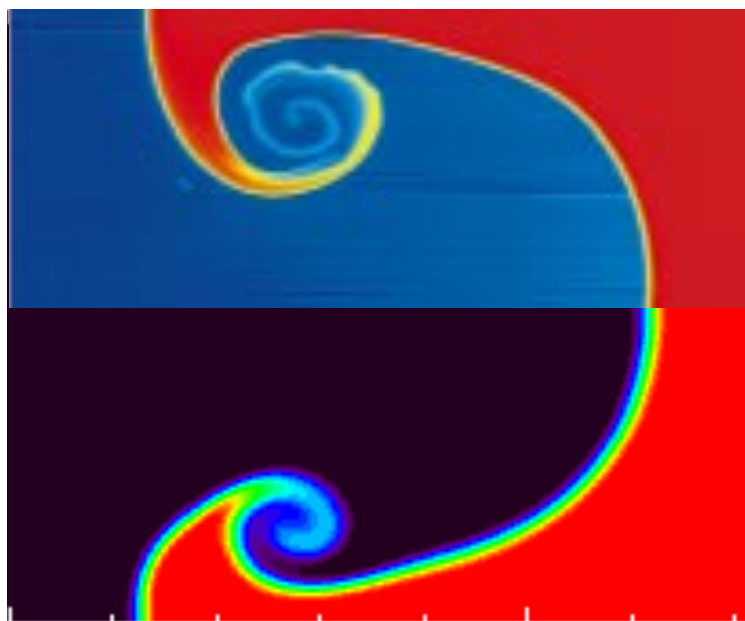
Figure 1.5: Comparison between experimental result and CRASH simulation for RMI. The upper panel is a PLIF image taken by B.D. Collins & J.W. Jacobs, 6 ms after the shock hit the air/SF$_6$ interface, in their experiment using shock Mach number M=1.21 [6], and the lower panel is from CRASH simulation.

equations both numerically [62] and analytically [17, 59], and the resulting discrepancy with infinite relative error between the impulsive model and linearized solution in the special case of reflected rarefaction wave has since cast doubt on the fundamental soundness of the impulsive model [59]. Other modern results from experiments, numerical simulations, and theoretical models are similarly dogged with inconsistencies, even for the simple case of sinusoidal perturbation activated by a planar shock [23, 9].

Since the self-similar, subsonic tail of the blast wave is preceded by the shock front, the instability at the interface caused by blast wave can be more accurately described as RMI followed by RTI. That said, RTI dominates the dynamics of the interface at later time since its exponential growth rate overwhelms the quadratic growth rate of RMI.

1.2.3 Kelvin-Helmholtz Instability

KHI occurs in flows with parallel velocity shear, with either homogeneous or heterogeneous fluid. It underlies familiar patterns of gas giants like Saturn and Jupiter, where velocity shear naturally occurs due to the differential velocity from poles to the equator in planetary rotation. Occasionally, clouds shaped by KHI, sometimes referred to as "Kelvin-Helmholtz wave clouds" can be seen under favorable conditions (Figure 1.6). At the late stage of RTI and RMI, the parallel velocity shear also rises between developed bubbles and spikes, so KHI becomes relevant and generates the familiar mushroom cap like the one in Figure 1.5.

KHI in the context of laboratory astrophysics constitutes the thesis work of Eric C. Harding [21]. This thesis won't discuss KHI in detail, however, since the major motivation for this thesis work is the absence of KHI.

Figure 1.6: Kelvin-Helmholtz wave clouds over Monument, Colorado. Photo credit Terry Robinson, from The Cloud Collector's Reference.

1.3 Scaled Supernova Rayleigh-Taylor Instability

1.3.1 Supernova Rayleigh-Taylor (SNRT) Experiments

Based on the argument of Euler similarity [48, 26], scaled experiments relevant to the RTI during supernova have been performed since the late 1990s to explore a variety of dynamics from simple RTI with planar interface [45, 27, 25], interface coupling [28], RTI with spherical interface [11], to RTI with multimodal sinusoid perturbation [33, 35]. The most recent ones that replicate the RTI at the He-H interface in supernova 1987A were performed with the Omega Laser facility at Rochester in 2009, in which the target consists of carbonized resorcinol formaldehyde (CRF) (essentially low-density carbon) foam and polyimide ($C_{22}H_{10}O_5N_2$), enclosed in a tube about 0.9 mm in diameter. The lasers deposit about 4.5×10^3 J of energy in 1 ns on the polyimide side, creating a blast wave which drives RMI and subsequently RTI at the interface between materials, which are now ionized plasma (Figure 1.7).

In these experiments, the interface between materials is "seeded" in the sense that well-defined 2D or 3D sinusoidal perturbations were machined onto the surface of polyimide in contact with the CRF foam in order to have facilitated and defined

9
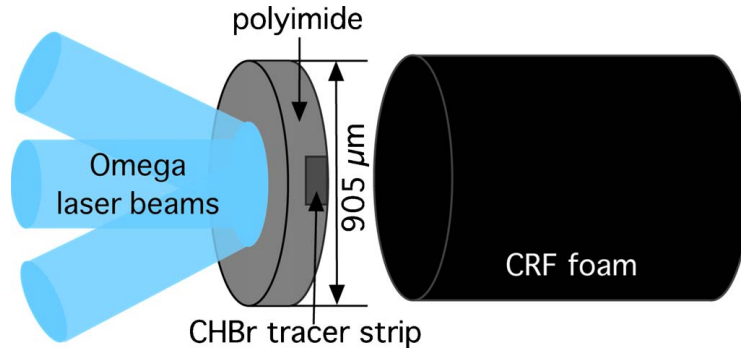
Figure 1.7: Diagram of the scaled SNRT experiment at the Omega Laser facility in 2009. CHBr tracer strip, with density (1.42 g/cm^3) close to that of polyimide (1.43 g/cm^3) is used to assist diagnosis, since polyimide is almost transparent to the x ray used in radiography. Figure from [34].
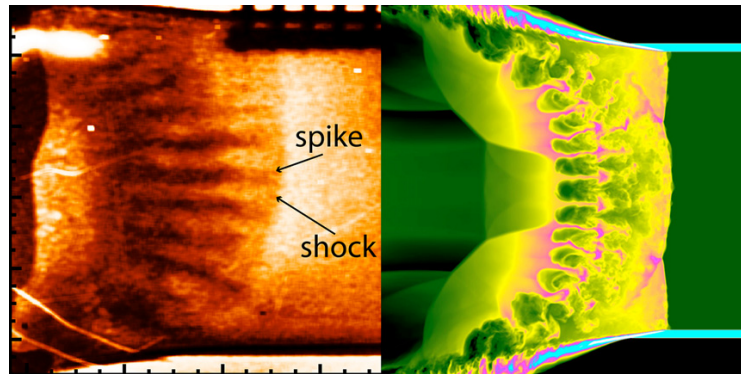
Figure 1.8: Comparison between the radiograph from the SNRT experiment and the simulation result from the FLASH code, courtesy of the FLASH Center for Computational Science at University of Chicago. Notice that the spikes in the experiment are of uniform width and lack the mushroom cap typical of late-time RTI. Figure from [18].

initial growth of the instability. In the end, however, KHI does not follow RMI and RTI for the ones with 3D sinusoidal perturbations as expected, and the spikes lack the typical mushroom caps. Furthermore, subsequent computer simulation also failed to reproduce such unusual morphology (Figure 1.8).

In response, a "Magnetic Straitjacket" hypothesis was proposed to explain the discrepancy, based on Biermann Battery mechanism [18].

1.3.2 Biermann Battery Mechanism, Magnetic Diffusion, and Magnetic Convection

Assuming that the dynamics of the electrons is fast compared to the dynamics of the fluid, ionized plasma without external magnetic field satisfies quasi-equilibrium:

$$\mathbf{E} = -\nabla P_e / e n_e \tag{1.2}$$

where n_e is the electron number density and e is the elementary charge. Applying Faraday's law

$$\frac{\partial \mathbf{B}}{\partial t} = -\nabla \times \mathbf{E} \tag{1.3}$$

and assuming ideal gas law $P_e = n_e k_B T_e$ for free electrons, we get

$$\frac{\partial \mathbf{B}}{\partial t} = (k_B / e)(\nabla T_e \times \nabla \ln n_e) \tag{1.4}$$

where k_B is the Boltzman's constant and T_e is the electron temperature. First proposed by Ludwig Biermann in 1950 [2], this means that misaligned gradients of electron temperature and number density in ionized plasma can seed magnetic field where it's initially absent, and experimentally magnetic field due to Biermann battery has been recently observed in a specifically designed RTI experiment during laser-ablation by Manuel et al. [40]. In the context of the SNRT experiment, it was proposed that longitudinal gradients along the bubble and spike in addition to the gradients across the material interface may result in azimuthal magnetic field, whose magnetic pressure ($B^2/2\mu_0$ in SI units, $B^2/8\pi$ in cgs units) keeps the spike in uniform width and mushroom cap from forming (Figure 1.9).

In such an evolving system with magnetic field, however, we have to take other terms into account. Firstly, the $\mathbf{E}$ field may not completely cancel out other forces
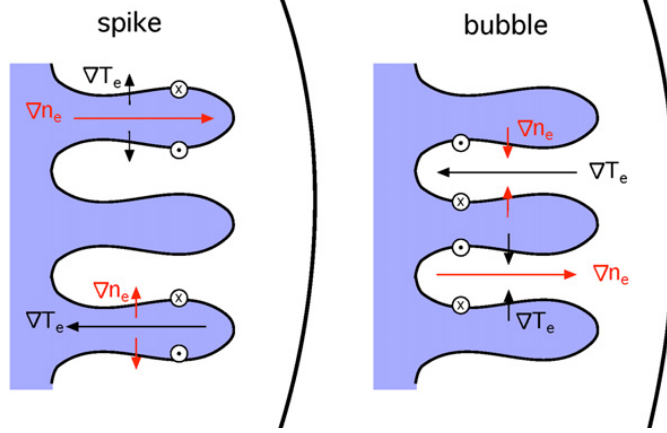
Figure 1.9: Diagram of the "Magnetic Straitjacket" hypothesis. Based on results of 1D simulations, longitudinal gradients and gradients across the material interface are proposed to produce azimuthal magnetic field, which acts like rubber bands and restricts the growth of KHI. Figure from [18].

acting on the electrons given that plasma is not a perfect conductor, and the resulting current $\mathbf{J}$ obeys Ohm's law $\mathbf{E}_{residual} = \mathbf{J}/\sigma$, where σ is the conductivity of the plasma. Secondly, moving electrons in $\mathbf{B}$ field obey Lorentz force law. Although this description is sufficient by itself, it is conceptually convenient to decompose the average velocity of the electrons into the current $\mathbf{J}/en_e$ component and the bulk velocity $\mathbf{u}$ of the plasma, and describe the force acting on the electrons due to the current $\mathbf{J}$ and magnetic field $\mathbf{B}$ as the Hall effect. Consequently, in SI units

$$\mathbf{E} = \underbrace{-\nabla P_e/en_e}_{\text{Quasi-equilibrium with } P_e} + \underbrace{\mathbf{J}/\sigma}_{\text{Ohm's law}} - \underbrace{\mathbf{u} \times \mathbf{B}}_{\text{Lorentz force}} + \underbrace{\mathbf{J} \times \mathbf{B}/en_e}_{\text{Hall effect}} \tag{1.5}$$

In particular, the resistive term due to Ohm's law results in diffusion of the magnetic field. Under quasi-equilibrium assumption, we expect displacement current $\epsilon_0 \frac{\partial \mathbf{E}}{\partial t}$ to be insignificant, so Ampere's law reads

$$\nabla \times \mathbf{B} = \mu_0 \mathbf{J} \tag{1.6}$$

So $\mathbf{J} = \nabla \times \mathbf{B}/\mu_0$,

12

$$\mathbf{E} = -\nabla P_e/en_e + \nabla \times \mathbf{B}/\mu_0\sigma - \mathbf{u} \times \mathbf{B} + (\nabla \times \mathbf{B}) \times \mathbf{B}/\mu_0 en_e \qquad (1.7)$$

Again with Faraday's law,

$$
\begin{aligned}
\frac{\partial \mathbf{B}}{\partial t} &= -\nabla \times \mathbf{E} \\
&= -\nabla \times (-\nabla P_e/en_e + \nabla \times \mathbf{B}/\mu_0\sigma - \mathbf{u} \times \mathbf{B} + (\nabla \times \mathbf{B}) \times \mathbf{B}/\mu_0 en_e)
\end{aligned}
\qquad (1.8)
$$

The last term is taken into account in the Hall MHD framework but not the standard MHD. We can estimate its magnitude relative to the Lorentz force term by replacing ∇ with the inverse of the length scale of the system $1/L$, and in our case the component of the average velocity of the electrons attributed to the current is negligible compared to the bulk velocity. Moreover, since magnetic field is divergence free, $\nabla \times (\nabla \times \mathbf{B}) = \nabla(\underbrace{\nabla \cdot \mathbf{B}}_{0}) - \nabla^2\mathbf{B}$,

$$\frac{\partial \mathbf{B}}{\partial t} = \underbrace{(k_B/e)(\nabla T_e \times \nabla \ln n_e)}_{\text{Biermann battery}} - \underbrace{\nabla^2\mathbf{B}/\mu_0\sigma}_{\text{magnetic diffusion}} + \underbrace{\nabla \times (\mathbf{u} \times \mathbf{B})}_{\text{magnetic convection}} \qquad (1.9)$$

So the resistivity of the plasma gives us magnetic diffusion, with diffusion constant $\eta = 1/\mu_0\sigma$. The ratio of the magnitude of the magnetic convection term to the magnitude of the magnetic diffusion term is the magnetic Reynolds' number R_m

$$R_m = \frac{|\nabla \times (\mathbf{u} \times \mathbf{B})|}{|\eta\nabla^2\mathbf{B}|} \qquad (1.10)$$

which can be estimated by replacing ∇ with $1/L$ and $\mathbf{u}$ with the typical velocity scale of the system U:

$$R_m = UL/\eta \qquad (1.11)$$

If $R_m \ll 1$, the local magnetic field quickly diffuses away. Conversely if $R_m \gg 1$, the

local magnetic field persists within the flow of the plasma, as is the case for the experiment by Manuel et al. Unfortunately in our system, R_m was estimated to be ~ 0.1 and dependent on the temperature, which is in turn dependent on resistive heating. As the Biermann battery term and magnetic diffusion term jointly determine the strength of the magnetic field, it is unclear whether the resulting magnetic pressure would be significant enough to influence the overall dynamics of the SNRT problem. Notice that although the SNRT experiments were intended to model the dynamics of layer mixing during a supernova explosion, the potential complications of the **B** field in the experiments do not necessarily apply to the dynamics of supernova. Indeed, as an example of the breakdown of scale invariance, the gradients of the electron temperature and number density are expected to be much smaller during the supernova layer mixing due to the vast spatial scale, so the resultant magnetic pressure is not expected to be significant relative to the ram pressure ρu^2 of the supersonic flow [18, 48].

1.4 Summary of Chapters

The goal of my thesis is to model the SNRT problem through simulations to test the Magnetic Straitjacket hypothesis. This introduction has stated the hypothesis we would like to test in the context of CFD, laboratory astrophysics, and hydrodynamic instabilities relevant to supernovae. In Chapter II, we introduce the CRASH code package and numerical methods used in this thesis. In Chapter III, we present the results of RTI simulations using CRASH. We have examined both the early-time and late-time behavior, and tested the low resolution limit of CRASH RTI simulations. The work for Chapter III was published in the journal *High-Energy-Density Physics* [5]. In Chapter IV, we present the work of CRASH RMI simulations, in comparison with the experimental data and the results of other code packages. With the code tested for such instabilities, Chapter V shows the results of 2D/3D CRASH simu-
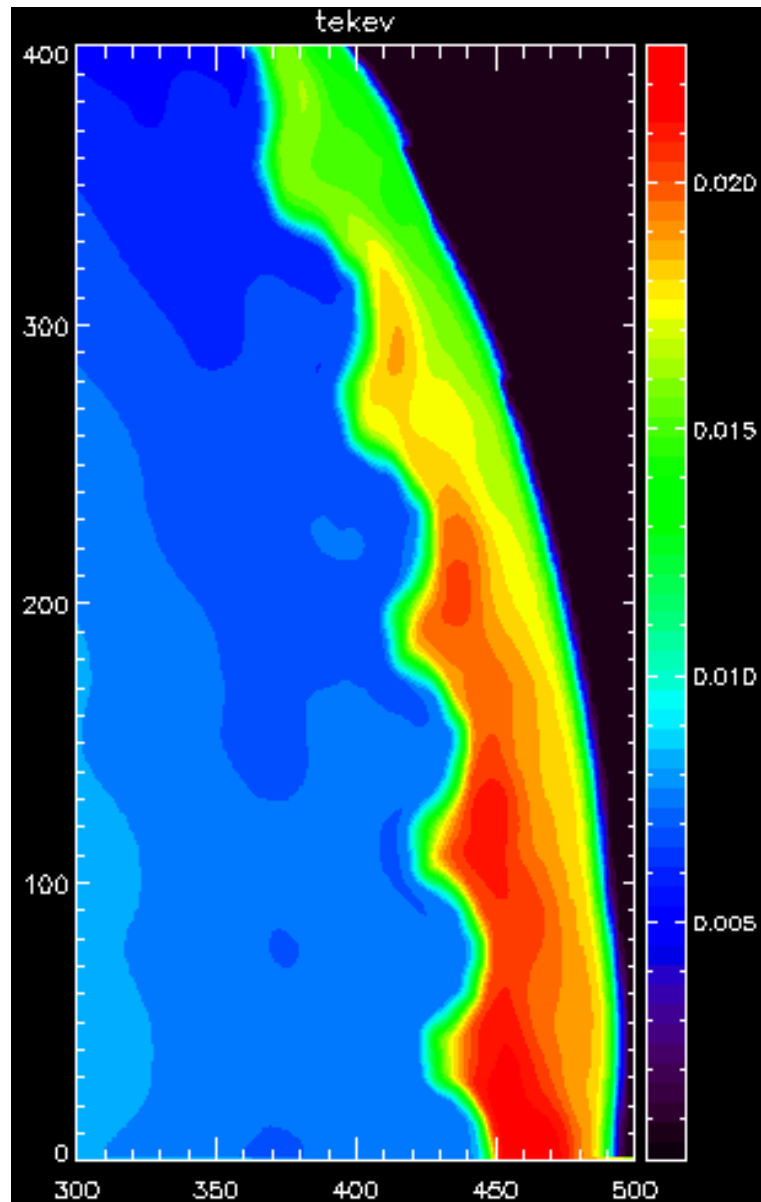
Figure 1.10: Snapshot of the electron temperature T_e at 7 ns, 2D CRASH simulation for the SNRT problem. Although the direction of the gradient across the material interface is as predicted, a longitudinal gradient within the (blue) spike, anticipated from 1D simulations, is notably absent at this time and on this scale of color mapping.

lations for the SNRT problem (Figure 1.10). We then draw the conclusions we can make and point out some of the potential future directions in Chapter VI.

CHAPTER II

CRASH Code Package and Numerical Methods

2.1   Background

The CRASH code was developed with the support of the Predictive Science Academic Alliance Program (PSAAP). Based on the Block-Adaptive Tree Solarwind Roe Upwind Scheme (BATS-R-US) code [55], the CRASH code incorporates additional capacities in order to model the radiative shock tube experiments performed at the Omega Laser facility (Figure 2.1 and 2.2) [56]. The decision to use the CRASH code for the SNRT problem was inspired by both its similarity to the originally intended problem and my earlier involvement in the main CRASH program [22, 41]. We will briefly describe the numerical methods and level set method used for this thesis and additional capabilities used for Chapter V in the following sections, and refer the readers to the bibliography for further details.

2.2   Numerical Methods

For this thesis, we only used CRASH's implementation of the HLLE scheme [15] and Godunov scheme [19] with an exact Riemann solver, both second order in space and time. An explicit 2-stage Runge-Kutta scheme with Courant-Friedrichs-Lewy (CFL) number 0.8 is used for time integration, and the flux is calculated with recon-
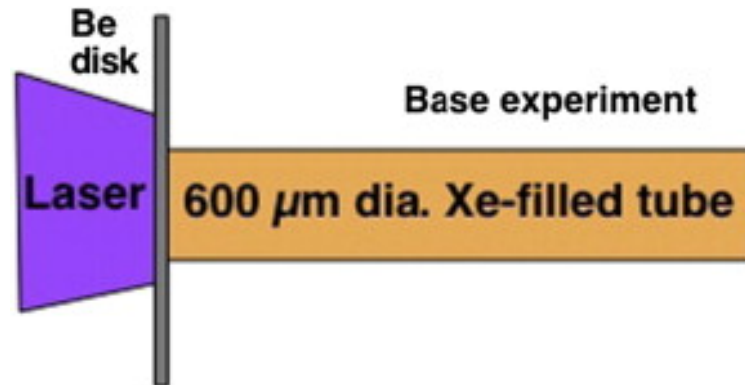
Figure 2.1: Diagram of the radiative shock tube experiment. 10 laser beams with a total energy of ~ 3.8 kJ irradiate a 20-μm-thick beryllium disk, and the ablated Be in turn drives the primary shock through the shock tube filed with Xe. The ablated Be loses significant energy due to thermal radiation, which passes through the optically-thin pre-shock Xe, preheats the plastic wall, and induces secondary wall shock. The plastic wall consists of the same material as the disk used in the SNRT experiments, polyimide. Figure from [57].
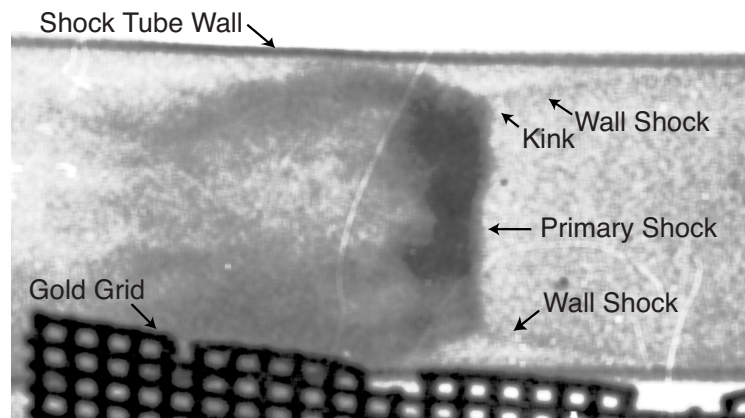
Figure 2.2: Experimental observation of the radiative shock tube experiment. Both the primary shock and wall shock are clearly visible. The gold grid is for instrument calibration, and the kink results from the interactions between the primary shock and the wall shock. Figure from [10].

structed linear slopes of the state variables within cells, using generalized monotonized central limiter or generalized Korens limiter [31]. A flux limiter is required for these Riemann solvers to extrapolate the state variable U from the left and right cell centers to the cell face at $i + 1/2$ for these schemes as

$$U^L_{i+1/2} = U_i + \frac{1}{2}\overline{\Delta}U_i,$$

$$U^R_{i+1/2} = U_{i+1} - \frac{1}{2}\overline{\Delta}U_{i+1},$$

where $\overline{\Delta}U_i$ is the limited slope in cell i. For the generalized monotonized central (mc) limiter, $\overline{\Delta}U_i$ is given by

$$\overline{\Delta}U_i = \text{minmod}\left[\beta(U_{i+1} - U_i), \beta(U_i - U_{i-1}), \frac{U_{i+1} - U_{i-1}}{2}\right]$$

The limited slopes in the left and right extrapolations are constructed asymmetrically for the generalized Koren's (mc3) limiter as

$$\overline{\Delta}^L U_i = \text{minmod}\left[\beta(U_{i+1} - U_i), \beta(U_i - U_{i-1}), \frac{2U_{i+1} - U_i - U_{i-1}}{3}\right]$$

$$\overline{\Delta}^R U_i = \text{minmod}\left[\beta(U_{i+1} - U_i), \beta(U_i - U_{i-1}), \frac{U_{i+1} - U_i - 2U_{i-1}}{3}\right]$$

In both cases, β is an adjustable parameter which controls the amount of numerical dissipation with range $1.0 \leq \beta \leq 2.0$.

2.3   Level Sets and Material Identification

For the simulations presented in this thesis, level set method is used to distinguish the identity of the fluids. For example, two level set functions are set up such that Initially $d_{Be} = 1$ and $d_{Xe} = -1$ where the heavy fluid is present, and $d_{Be} = -1$ and $d_{Xe} = 1$ where the light fluid is present for the RTI simulations. The level set

functions d_m are then advected along with the state variables according to the simple advection equation [56]

$$\frac{\partial d_m}{\partial t} + \nabla \cdot (d_m \mathbf{u}) = d_m \nabla \cdot \mathbf{u}$$

where m is one of the two arbitrary labels "Be" and "Xe", conveniently chosen since they are two of the elements used in the main CRASH program. Up to 5 different fluids (therefore 5 level set functions) can be used simultaneously, as is the case for the 2D SNRT simulations presented in Chapter V. The identity of the fluid in a cell is then determined by its most positive level set function through the winner-take-all algorithm. Consequently, a cell never contains two different fluids at the same time.

2.4   Radiation Transport

Radiation transport in CRASH is modeled as flux-limited gray or multi-group diffusion [56]. For the multi-group diffusion, the total radiation energy density is divided into radiation energy densities for intervals of photon frequencies, $[\nu_{g-1/2}, \nu_{g+1/2}]$:

$$E_g = \int_{\nu_{g-1/2}}^{\nu_{g+1/2}} E_\nu d\nu \tag{2.1}$$

where E_ν is the spectral energy density, $g = 1, \ldots, G$, and G denotes the number of groups. The groups are logarithmically distributed in frequency such that $\ln(\nu_{g+1/2}) - \ln(\nu_{g-1/2})$ is constant. The radiation energy density in each group then evolves according to the diffusion equation

$$\frac{\partial E_g}{\partial t} \;+\; \underbrace{\nabla \cdot (E_g \mathbf{u})}_{\text{advection}}$$

$$+ \;\; \underbrace{(\gamma_r - 1)\nabla \cdot \mathbf{u}\left(E_g - \int_{\nu_{g-1/2}}^{\nu_{g+1/2}} \frac{\partial(\nu E_\nu)}{\partial \nu} d\nu\right)}_{\text{compression}}$$

$$= \;\; \underbrace{\nabla \cdot (D_g \nabla E_g)}_{\text{diffusion}} + \underbrace{\sigma_g (B_g - E_g)}_{\text{emission - absorption}} ,$$

$$D_g \;=\; c/(3\kappa_{R_g}),$$

$$\sigma_g \;=\; c\kappa_{P_g} \tag{2.2}$$

where $\gamma_r = 4/3$ is the adiabatic index of the photon gas, c is the speed of light, B_g is the energy flux of the blackbody radiation within the radiation group g, κ_{R_g} and κ_{P_g} are the Rosseland mean opacity and Planck mean opacity for the radiation group g, respectively. When only one radiation group is used with radiation energy density $E_r = \int_0^\infty E_\nu d\nu$, the treatment above reduces to single group approximation, usually referred to as gray radiation diffusion:

$$\frac{\partial E_r}{\partial t} + \nabla \cdot (E_r \mathbf{u}) + (\gamma_r - 1)E_r \nabla \cdot \mathbf{u} = \nabla \cdot (D_r \nabla E_r) + \sigma_r (B - E_r) \tag{2.3}$$

where $B = aT_e^4$ is the total energy flux of the blackbody radiation with Stefan-Boltzmann constant $a = \frac{2\pi^5 k_{\mathrm{B}}^4}{15 h^3 c^2}$, given the electron temperature T_e.

As it is, the radiation diffusion flux $\mathbf{F}_g = -D_g \nabla E_g$ may exceed the free-streaming limit cE_g if the Rosseland mean opacity is sufficiently low. The square-root flux limiter [42] is therefore employed in CRASH which modifies the diffusion constant D_g as

$$D_g = \frac{c}{\sqrt{(3\kappa_{Rg})^2 + \frac{|\nabla E_g|^2}{E_g^2}}} \tag{2.4}$$

21

in order to keep the radiation diffusion from transporting energy faster than light.

The capacity of radiation transport is central to the main CRASH program. Although radiation transport is not expected to be significant for the dynamics of the instability for the SNRT problem, we found that the shock velocity is sensitive to the presence of radiation transport, presumably due to the energy loss during laser ablation. Consequently, the SNRT simulations presented in Chapter V employ multigroup radiation transport.

2.5   Electron Heat Conduction

The implementation of electron heat conduction in CRASH is based on the classical Spitzer-Harm formula, where the heat flux due to the electrons is given by

$$
\begin{aligned}
\mathbf{F} &= -C_e \nabla T_e, \\
C_e &= \chi \rho c_p
\end{aligned}
\tag{2.5}
$$

where ρ is the mass density of the plasma, c_p is the specific heat at constant pressure, and χ is the heat diffusion constant whose dimension is the expected length^2 time^{-1}. In units typical for laboratory astrophysics [12],

$$
\chi(\mathrm{cm}^2\mathrm{s}^{-1}) = 3.3 \times 10^{-3} \frac{A[T(\mathrm{eV})]^{5/2}}{\ln\Lambda \bar{Z}(\bar{Z}+1)\rho(\mathrm{g\ cm}^{-3})}
\tag{2.6}
$$

where A is the average atomic mass, $\bar{Z}$ is the average ionization, and $\ln\Lambda$ is the Coulomb logarithm. This collisional model, however, gives unphysical result when the scale of the temperature gradient $T_e/|\nabla T_e|$ is no longer much larger than the mean free path of the electrons. At the free-streaming limit, the magnitude of the electron heat flux is instead given by $F_{FS} = n_e k_B T_e v_{th}, v_{th} = \sqrt{k_B T_e/m_e}$, m_e being

the mass of the electron. The final form of the electron heat flux is therefore flux-limited as follows [56], similar to the approach taken for the radiation transport:

$$\mathbf{F} = -\min\left(C_e, \frac{f F_{FS}}{|\nabla T_e|}\right)\nabla T_e \tag{2.7}$$

where the flux limiter f is a tunable numerical parameter. f is typically set to be 0.06 for the main CRASH program and is unchanged for our SNRT simulations.

2.6 EOS and Opacity

Although the CRASH code is completed with internal EOS solvers and opacity models for the materials used in the main CRASH program [52], the properties of the plasma necessary for the simulation are not calculated on the fly for efficiency reason. Instead, the values for these properties are tabulated beforehand, and the CRASH code looks them up from the table in the course of simulation. The lookup arguments for the EOS tables are the logarithms of electron temperature and atomic number density $(\log T_e, \log n_a)$, whereas the lookup arguments for the specific Rosseland mean opacity κ_{R_g}/ρ and specific Planck mean opacity κ_{P_g}/ρ for a given radiation group g are the logarithms of mass density and electron temperature $(\log \rho, \log T_e)$ [56].

Another advantage of this tabular approach is the flexibility to use alternative EOS and opacity models. In our case, the polyimide EOS table given by the CRASH internal solver turned out to be ill-suited for the SNRT problem, since the average ionization $\bar{Z}$ is not monotonic with respect to T_e when the atomic number density is above $\sim 10^{27}$ m^{-3} (Figure 2.3). Early attempts of SNRT simulations using the CRASH EOS table for polyimide were consequently affected by oscillations in T_e, since the electron temperature is not uniquely determined by the pressure and density (Figure 2.4). This issue is resolved after switching to the EOS table given by PROPACEOS, whose $\bar{Z}$ is always monotonic with respect to T_e (Figure 2.5).
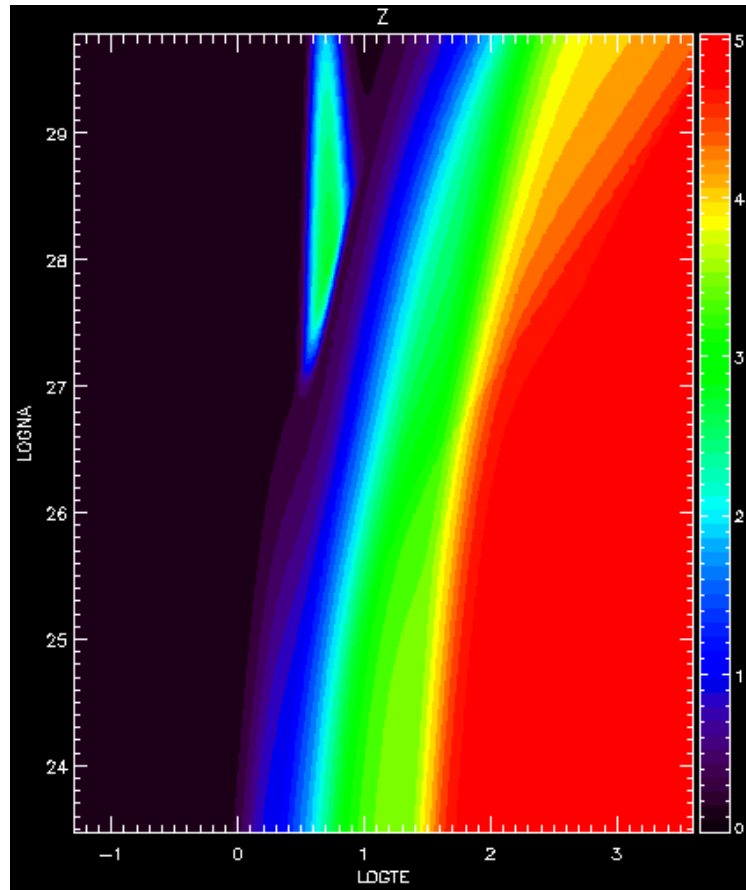
Figure 2.3: Average ionization $\bar{Z}$ of the polyimide plasma given by the CRASH internal EOS solver as a function of $\log T_e(\mathrm{eV})$ and $\log n_a(\mathrm{m}^{-3})$, one of the EOS properties whose values are tabulated.
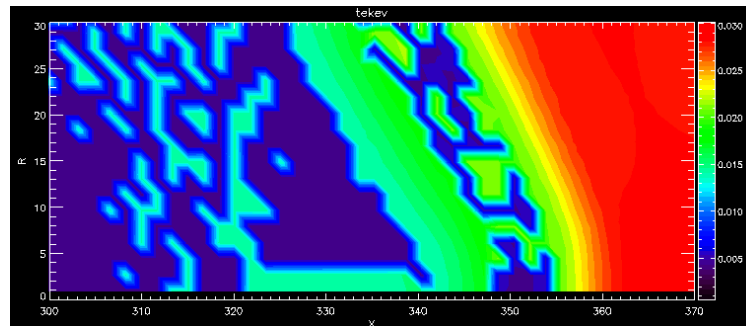
Figure 2.4: T_e (keV) snapshot of the center spike at $t = 5$ ns, 2D SNRT simulation using the CRASH EOS table for polyimide. The electron temperature T_e of the polyimide plasma oscillates between the two possible solutions.
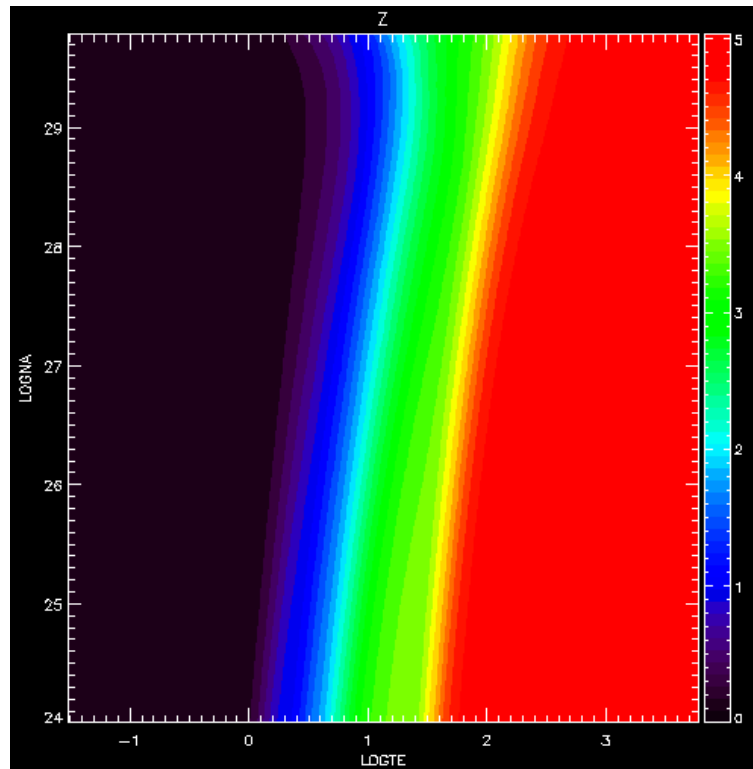
Figure 2.5: Average ionization $\bar{Z}$ of the polyimide plasma given by PROPACEOS as a function of $\log T_e(\mathrm{eV})$ and $\log n_a(\mathrm{m}^{-3})$.

2.7   Laser Energy Deposition Library

Lastly but crucially, a laser package was added to the CRASH code, which models the transport and deposition of the laser energy. The former is approximated by a ray-tracing algorithm based on geometric optics, while the later primarily occurs through inverse Bremsstrahlung physically and is modeled exclusively as inverse Bremsstrahlung along the trajectory of the rays [57]. We used this laser package for the SNRT simulations after adopting it for our laser configuration and polyimide average atomic mass $A_r = 9.80326205$ (instead of 9.0121823 for the Beryllium used in the main CRASH program).

CHAPTER III

Rayleigh-Taylor Instability Simulations with CRASH

3.1 Introduction

As the first step towards modeling the unusual morphology observed in SNRT experiments [18], the results of RTI simulations with CRASH are reported in this chapter. We performed simple hydrodynamics simulation on a fixed 2D Cartesian grid as we examined three different regimes (linear early-time behavior, late-time morphology, and low-resolution limit) of the physical and computational parameter space and compared the effects of different solvers, numerical parameters, and grid resolutions with respect to the analytical result and established expectations.

3.2 Linear Early-time Behavior

In the simplest case with discontinuous interface and a 2D single-mode perturbation that is small in amplitude relative to the wavelength λ, linear theory predicts that the mixing zone width of the RTI grows exponentially as

$$\text{width} \propto \exp(\gamma t),$$

$$\gamma = \sqrt{Agk}, \, A = \frac{\rho_2 - \rho_1}{\rho_2 + \rho_1}$$

where A is the Atwood number, g is the gravitational acceleration, and k is the wavenumber $2\pi/\lambda$. For this study, we nominally set $\rho_2 = 1000$ kg/m^3, $\rho_1 = 500$ kg/m^3, $A = 1/3$, $g = 9806.65$ m/s^2, and $\lambda = 0.0002$ m.

The simulation is set in a 2D square box with length equal to λ and gravity pointing to the left. The boundary condition is periodic, except at the left and right edges where reflective boundary condition is necessary to support and isolate the fluids. The minimum pressure of the system is $p_{min} = 10^5$ Pa and the pressure increases along the direction of gravity in order to maintain hydrostatic equilibrium. Both light and heavy fluids are set to follow the ideal gas equation of state with $\gamma = 5/3$, but they are nonetheless labeled with different material indices such that their motion can be tracked accurately with the level set method implemented in CRASH. With the heavy fluid conveniently labeled as "Be", the mixing zone width is defined as the horizontal distance from the tip of the spike to the top of the bubble, which are in turn defined as the leftmost extent of the heavy fluid (where $d_{Be} > 0$) and the rightmost extent of the light fluid (where $d_{Be} < 0$). The instability is initialized with velocity field

$$u_x(x, y) = \cos(ky) \times \exp\left(-\frac{1}{2}\left(\frac{x - x_{interface}}{\lambda/2e^4}\right)^2\right) \times u_{init}$$

which perturbs the interface in a sinusoidal pattern but vanishes rapidly away from the interface. Here e is the the base of the natural logarithm and u_{init} is one thousandth of the speed of sound at the right edge:

$$u_{init} = 0.001c = 0.001 \times \sqrt{\frac{5}{3}\frac{p_{min}}{\rho_2}} \sim 0.0129 \text{ m/s}$$

Since the behavior of the system without viscosity does not depend on the length scale, we can simply express the mixing zone width as a fraction of the wavelength
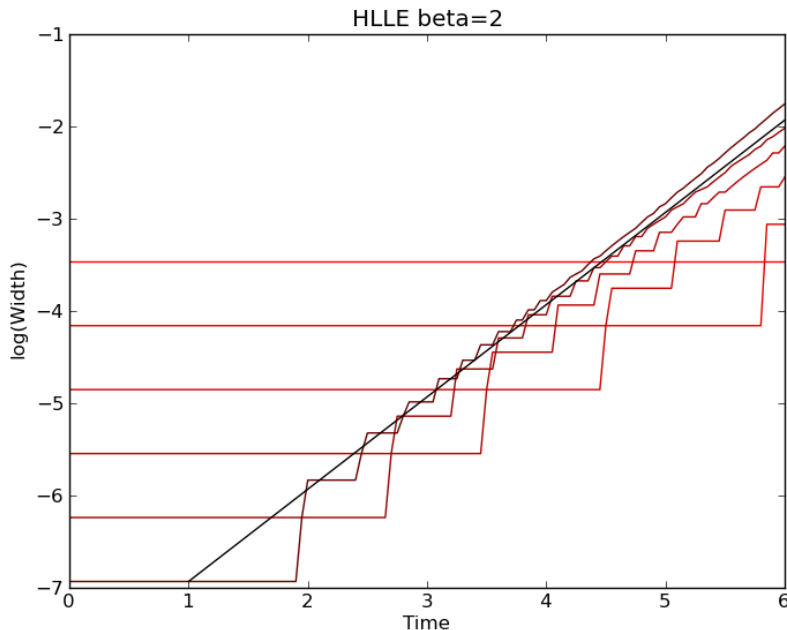
Figure 3.1: Mixing zone width vs. time, HLLE scheme, mc limiter, $\beta = 2.0$. Darker color indicates higher resolution as number of cells per wavelength, which ranges from 2^5 to 2^{10}. The black line marks the linearized analytical result with slope $= 1$.

and use the dimensionless time γt to plot the logarithm of the mixing zone width over time. Figure 3.1 depicts the result for the HLLE scheme with $\beta = 2.0$, while Figure 3.2 depicts the result for the Godunov scheme with $\beta = 1.0$ (mc limiter is used for both cases). Lines with darker color indicate higher resolution as number of cells per wavelength, and the black line marks the linearized analytical result, which is simply a straight line with slope 1 in the semi-log plot with normalized units.

After the instability overcomes the numerical dissipation, its growth rate follows the linearized analytical result. It deviates again later in time for high-resolution runs, however, especially in the case of the Godunov scheme with the exact Riemann solver. Examination of the level-set plots of the heavy fluid "Be" at the end of the simulation with the highest resolution (Figure 3.3 and 3.4) reveals that this is due to the spontaneous growth of smaller-wavelength instabilities, whose presence is un-
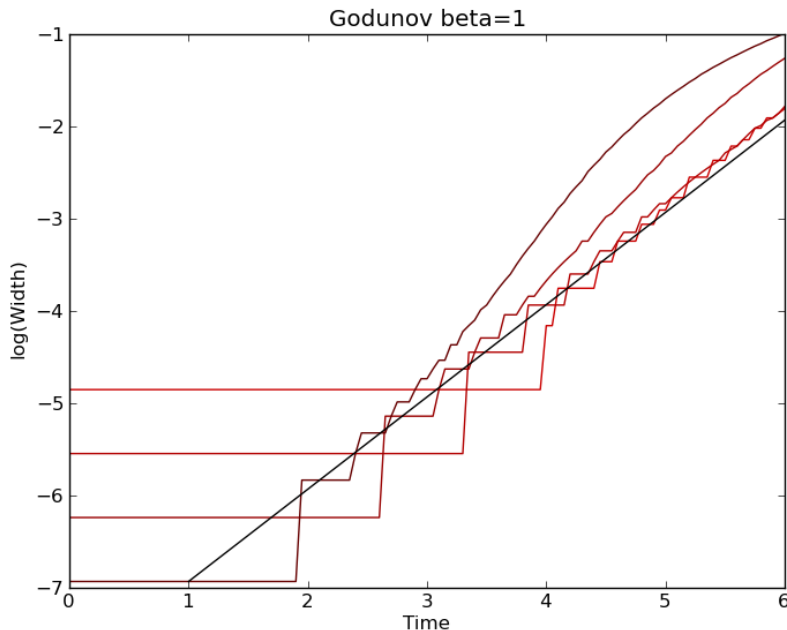
Figure 3.2: Mixing zone width vs. time, Godunov scheme, mc limiter, $\beta = 1.0$ with resolution from 2^7 to 2^{10}. The black line marks the linearized analytical result with slope $= 1$.

avoidable, as the initial perturbation can't be perfectly sinusoidal on a Cartesian grid, and the numerical error will grow exponentially due to the very nature of the system. Since small-wavelength instabilities grow faster in this regime without physical viscosity, they corrupt the growth of the intended long-wavelength instability after several natural time units. In the extreme case of Godunov scheme with 1024 cells per wavelength, we can see that small-wavelength instabilities already developed a complicated pattern of spikes and bubbles with fully developed mushroom caps, while the long-wavelength instability is still in the linear regime.

3.3 Late-time Morphology

Although the early-time behavior has the advantage of having a linearized analytical result that can be used for reference, the late-time morphology is perhaps more relevant for our purpose. For these runs, we used a moderate single-mode geome-

30
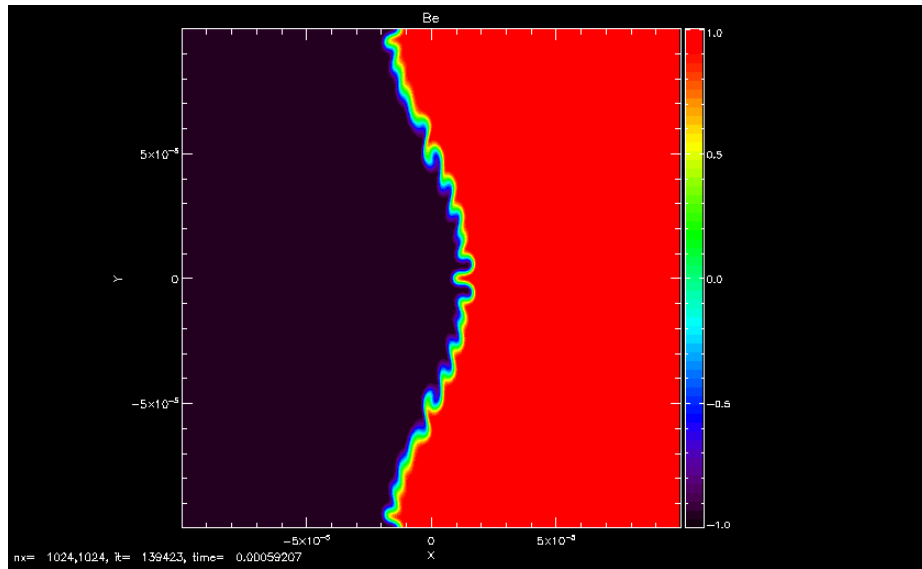
Figure 3.3: Level-set plot at the end of the simulation ($t = 6$ natural time unit), HLLE scheme, 1024 cells per wavelength. Smaller-wavelength instabilities outpace and corrupt the growth of the intended long-wavelength instability. Gravity points to the left, and the spike grows along the upper and lower edges of the grid.
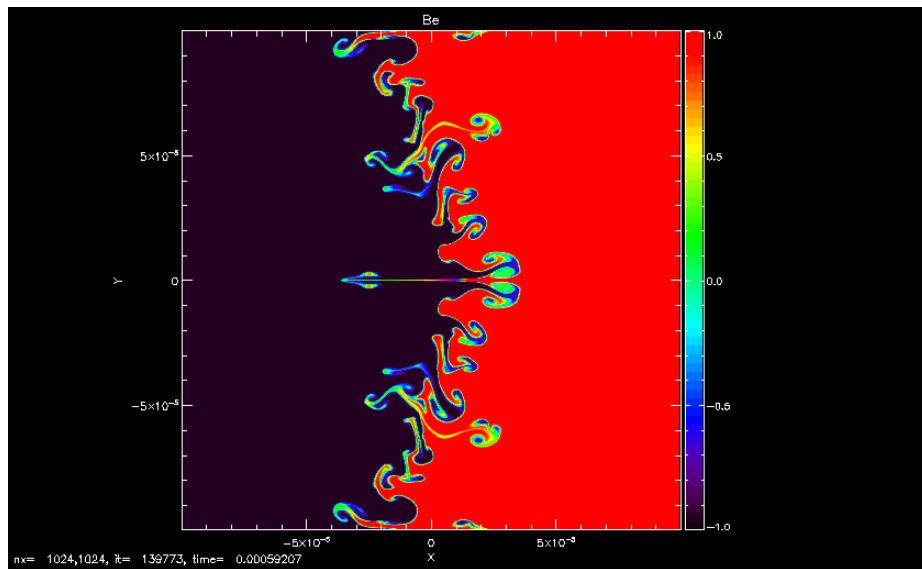
Figure 3.4: Level-set plot at the end of the simulation ($t = 6$ natural time unit), Godunov scheme, 1024 cells per wavelength. Small-wavelength instabilities are even more prominent in this case because the exact Riemann solver has less numerical dissipation.
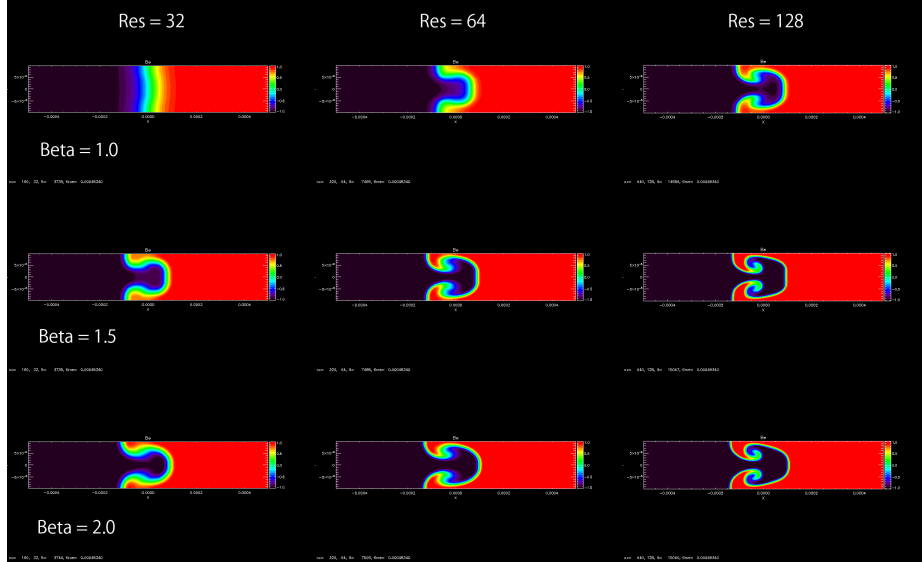
Figure 3.5: Level-set morphology grid for the HLLE scheme. The resolution as number of cells per wavelength is fixed for each column, and the value of β is fixed for each row.

try perturbation instead of a velocity perturbation: the interface is set up as a sine wave with amplitude $= \lambda/2e^4$, with the rest of the parameters the same. Figure 3.5 and 3.6 depict the result after 5 natural time units as two 3×3 morphology grids for the HLLE scheme and Godunov scheme, respectively. The resolution as number of cells per wavelength is fixed for each column and ranges from 32 to 128, and the value of β is fixed for each row and ranges from 1.0 to 2.0.

Figure 3.5 shows that the growth of the mushroom cap (Res $= 32$ with $\beta = 1.5 \sim$ 2.0, Res $= 64$ with $\beta = 1.0$), and in the extreme case the instability itself (Res $= 32$ with $\beta = 1.0$), can be impeded for the HLLE scheme. While mushroom caps can be seen in all of the rest of the runs, only the two runs with the least numerical diffusion (Res $= 128$ with $\beta = 1.5 \sim 2.0$) show the roll up. The Godunov scheme (Figure 3.6) has the opposite problem. The high-resolution and high-beta runs generate various unphysical artifacts which we attribute to insufficient numerical viscosity. A dimple at the top of the bubble is clearly visible in runs Res $= 64$ with $\beta = 1.5 \sim 2.0$, and all of the runs with Res $= 128$ develop three layers of KHI. When the progress of
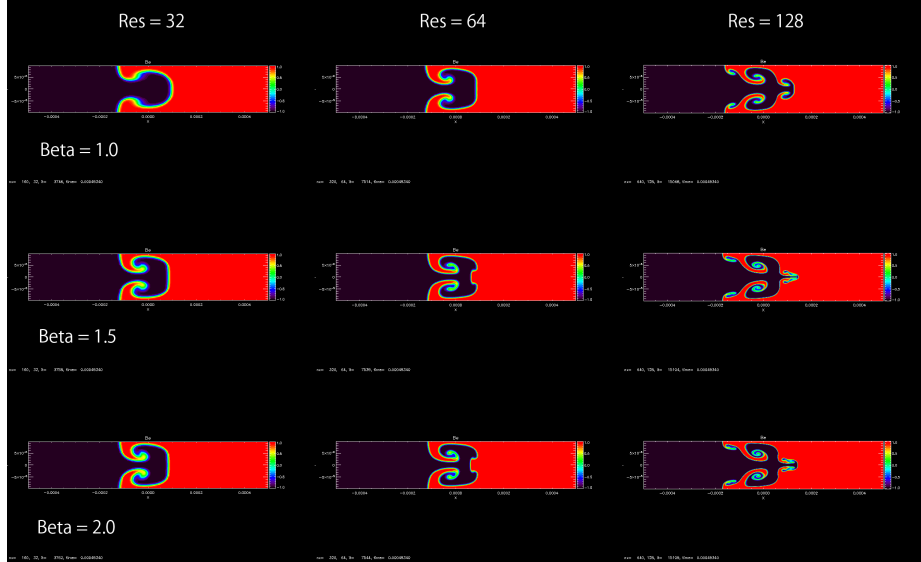
Figure 3.6: Level-set morphology grid for the Godunov scheme. The resolution as number of cells per wavelength is fixed for each column, and the value of β is fixed for each row.

the instability growth is examined in detail, e.g., the Res = 128 with $\beta = 2.0$ case in Figure 3.7, we can see that this is simply another manifestation of the corruption due to the extraneous small-scale features. In fact, even more features were generated by the small-wavelength RTI and KHI, but several of them merged with each other, and only three layers of KHI survived.

3.4   Low-resolution Limit

We varied the amplitude of the geometry perturbation from 0.025 to 0.2, β from 1.0 to 2.0, resolution as number of cells per wavelength $= 8, 16$, and 24, Atwood number $1/10 \sim 1/2$, and tested both the HLLE scheme and Godunov scheme with both mc and mc3 limiter. It turned out that the growth of the instability with the Godunov scheme is robust against these variations of parameters, but the more diffusive HLLE scheme requires the resolution to be > 16 for the instability to grow (Table 3.1).

Some of the exploratory simulation runs indicate that the growth of the instability is more robust when the interface is perturbed by a small velocity field instead. This
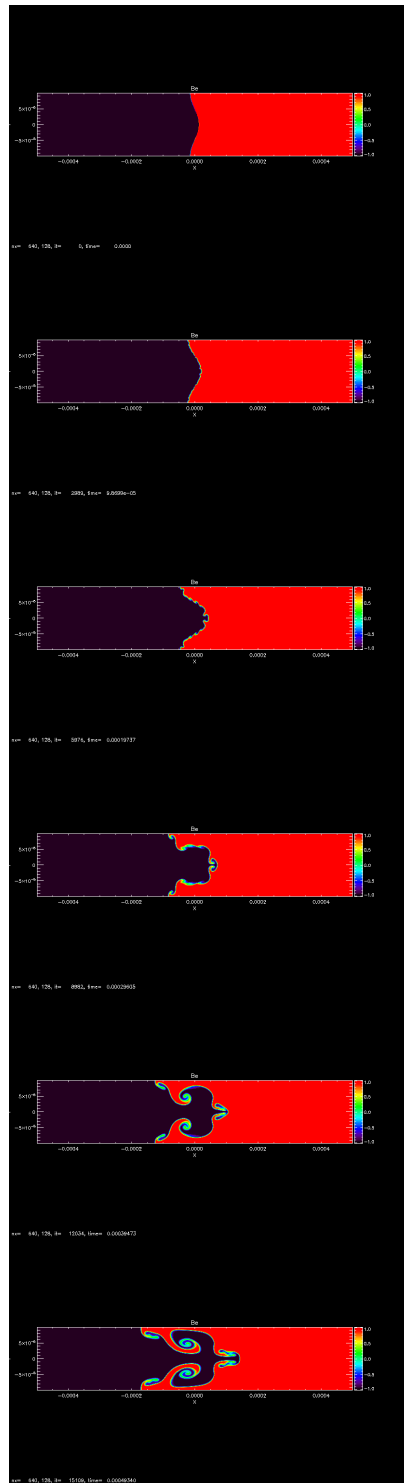
Figure 3.7: Detailed progress of the morphology evolution for the Godunov scheme, with configuration corresponding to the lower-right corner of the morphology grid (Res = 128 with β = 2.0). Snapshots were taken at $t = 0, 1, 2, 3, 4, 5$ natural time units.

HLLE	Res=8	Res=16	Res=24
$\beta = 1.0$	No Growth	No Growth	Growth
$\beta = 1.5$	No Growth	No Growth	Growth
$\beta = 2.0$	No Growth	No Growth	Growth

Table 3.1: Results of CRASH RTI simulations with HLLE scheme at low-resolution limit

is not unexpected: the density gradient in geometry perturbation diffuses away with time in HLLE scheme, but the velocity perturbation is protected by the conservation of momentum and energy.

3.5   Conclusions

We found that CRASH is capable of reproducing reasonable behavior in RTI simulation, despite the fact that the original code base was neither designed nor tested for such hydrodynamic instability. For the early-time behavior, the growth rate converges to the analytical result, although the lack of physical viscosity model allows high resolution runs to be complicated by the smaller-wavelength, secondary instabilities. Similarly, CRASH generates expected late-time morphology for RTI, given the appropriate choice of numerical scheme, resolution, and limiter beta. Finally, the low-resolution limit for RTI growth in CRASH's numerical schemes can provide a lower bound for the required resolution in simulations where RTI is expected to play an important role.

CHAPTER IV

Richtmyer-Meshkov Instability Simulations with CRASH And Cross-Code Comparison

4.1 Introduction

As the next step towards SNRT instability simulation [18], we used CRASH to model the mach number $M_s = 1.21$ case of Collins and Jacobs' RMI experiment [6] and compared the result with those of other code packages including DAFNA (hydrodynamic AMR code developed in Nuclear Research Center NEGEV, see [39, 61] for its applications) and HUM3D (code developed by University of Michigan professor Eric Johnsen's group). Collins and Jacobs' result is chosen as the experiment to model because it's frequently used as the yardstick for RMI simulations with various code packages and numerical methods [37, 32, 38] available for comparison.

4.2 Physical Parameters of The Experiment

Instead of the traditional method of setting up the interface between two fluids with membrane for RMI experiment, Collins and Jacobs' setup maintains the interface by flow stagnation. The two fluids, SF_6 and air-acetone mixture, are sent from the opposite ends of the shocktube and escape through slots at the designated location, forming a interface at the stagnation point flow. The interface is then seeded with
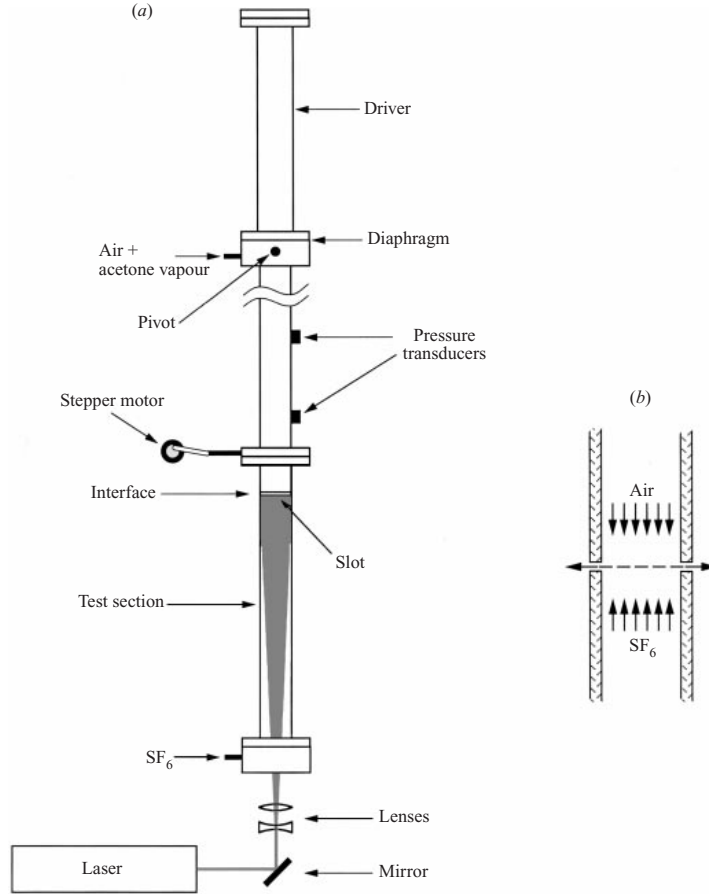
Figure 4.1: Setup of Collins and Jacobs' Experiment. The low-density air-acetone mixture and high-density SF_6 are sent from the top and bottom of the shocktube, respectively (a). The two fluids reach stagnation point flow at the designated location and are allowed to escape, forming an interface (b). Sinusoidal perturbation is then created at the interface by inducing a standing wave with a stepper motor. Figure from [6].

a sinusoidal perturbation by vibrations created by a stepper motor (Figure 4.1). By avoiding the use of a membrane in the setup, this experiment avoids its potential complications in instability growth and diagnosis. A diaphragm from the air-acetone side of the shocktube is then punctured to generate a shock, which initializes the RMI when it reaches the perturbed interface at $t = 0$. The instability develops until $t \sim 6$ ms, when the reflected expansion wave and incident shock reaccelerate the interface.

The system is modeled as a 2D rectangle shocktube with parameters summarized in Table 4.1: wavelength (λ), wavenumber (k), and single-mode sinusoidal pertur-

λ (m)	0.0594	$x_{interface}$ (m)	0.03	A	0.605
k (1/m)	105.77	$t_{reshock}$ (ms)	6.6	P (Pascal)	95600
a (m)	0.00183	$u_{i,shock}$ (m/s)	370.98	M_{air} (g/mol)	34.76
Lx (m)	0.78	Ma	1.21	M_{SF6} (g/mol)	146.05
Ly (m)	0.0594	ρ_{air} (kg/m^3)	1.351	γ_{air}	1.276
x_{shock} (m)	0.01	ρ_{SF6} (kg/m^3)	5.494	γ_{SF6}	1.093

Table 4.1: Parameters of Collins and Jacobs' experiment

bation amplitude (a, half of the peak-to-valley distance) of the perturbation at the interface, length (Lx) and width (Ly) of the shocktube, initial position of the shock (x_{shock}) and interface ($x_{interface}$), time of the re-shock ($t_{reshock}$) when the reflected shock reaccelerates the interface relative to the start of RMI ($t = 0$), the velocity ($u_{i,shock}$) and Mach number (Ma) of the incident shock, the pre-shock densities of air-acetone mixture (ρ_{air}) and SF$_6$ (ρ_{SF6}), pre-shock Atwood number (A), pre-shock pressure (P), and average molecular weights of air-acetone mixture (M_{air}) and SF$_6$ (M_{SF6}). Air-acetone mixture and SF$_6$ are modeled as ideal gamma law gases with $\gamma_{air} = 1.276$ [37] and $\gamma_{SF6} = 1.093$. Note that not all simulations use all of these parameters: for example, molecular weights are ignored in CRASH simulations.

4.3   Simulation Setup and Numerical Parameters

In simulations, the top of the shocktube $x = 0$ through which the shockwave is sustained by the driver is modeled with inflow (non-reflective) boundary condition. All the other boundaries of the 2D rectangle shocktube are modeled with reflective (wall) boundary condition.

The CRASH simulations employed the HLLE scheme [15] and generalized Koren's limiter [31] with $\beta = 2.0$, as described in Section 2.2. DAFNA simulations employed the HLLC scheme [54], and HUM3D switches between a central scheme and a shock-capturing scheme [43]. We performed the simulations across all three code packages with three predetermined resolutions: 64, 128, and 256 cells per wave-

length (PWL). For the CRASH simulations, the same level set method for the RTI simulations (Sec. 2.2) is employed again to enable accurate tracking of the material and measurement of the instability amplitude, defined as half of the vertical distance between the uppermost extent of the SF_6 and lowermost extent of the air-acetone mixture, in the experiment frame.

4.4   Results

Morphologies of the instability given by the CRASH simulations are plotted and compared to the planar laser-induced fluorescence (PLIF) image from the experiment at $t = 6$ ms in Figure 4.2, from which we can see that the instability amplitude and morphology converge to the experimental result as we increase the resolution. Compared to Figure 3.5, however, we can see that the results of the CRASH simulations of the Jacobs experiment are more affected by numerical material diffusion even though the post-shock dynamics are similar to those of the RTI morphology runs. Qualitatively, the morphologies given by the CRASH simulations of the Jacobs experiment resemble those of the RTI morphology runs with the same numerical scheme and β but half of the resolution. Given that the numerical material diffusion is limited by the sound speed and that it's effect on the dynamics of the system is relative to the wavelength, we can calculate the time scale of numerical diffusion's effect on the system $\tau = \lambda/c$. For the CRASH RTI morphology runs, $\tau \sim 2^{-4}$ (m) $/\sqrt{\frac{5}{3}\frac{p_{min}}{\rho_1}}$ (m/s) ~ 10.95 ms and the morphologies of the instability are observed at ~ 0.045 τ. For the CRASH simulations of the Jacobs experiment, however, post-shock sound speed of the light fluid gives us $\tau \sim 0.0594$ (m) $/\sqrt{\gamma_{air}\frac{145348.25}{1.872}}$ (m/s) ~ 0.1887 ms, so the morphologies are observed at ~ 31.79 τ. We can't compare these two sets of simulations quantitatively without further knowledge since the width of the diffused interface doesn't grow linearly with time, but the drastic difference in observation time scaled by τ explains the different extent of the effect due to numerical material

Figure 4.2: From top to bottom: SF$_6$ level set plot of the instability at $t = 6$ ms given by the CRASH simulation with resolution = 64, 128, and 256 cells per wavelength respectively. The position along the x-axis is in the unit of meters due to internal normalization. The insets are the PLIF image from the experiment [6] taken at $t = 6.006$ ms for comparison.

diffusion.

In comparison, morphologies of the instability given by DAFNA are plotted and compared to the experiment in Figure 4.3. We can see that the HLLC scheme used by DAFNA is less affected by numerical material diffusion, but consequently with more visible discretization error. The curl-up of the mushroom cap appears more irregular than the experimental image, but no physical noise is present in the simulations.

Finally, instability amplitude over time given by CRASH, DAFNA, and HUM3D is plotted and compared to the experiment in Figure 4.5. The results for RMI prior to the re-shock seem to converge for all three code packages, although CRASH does require higher resolution due to its higher numerical material diffusivity. Given the spread of the experimental data points, the numerical results also seem to be consistent with the experiment. No agreement is achieved for instability amplitude after re-shock, however, due to the presence of 3D-turbulence in the experiment. The simulations have neither the necessary dimensionality nor the numerical model to handle
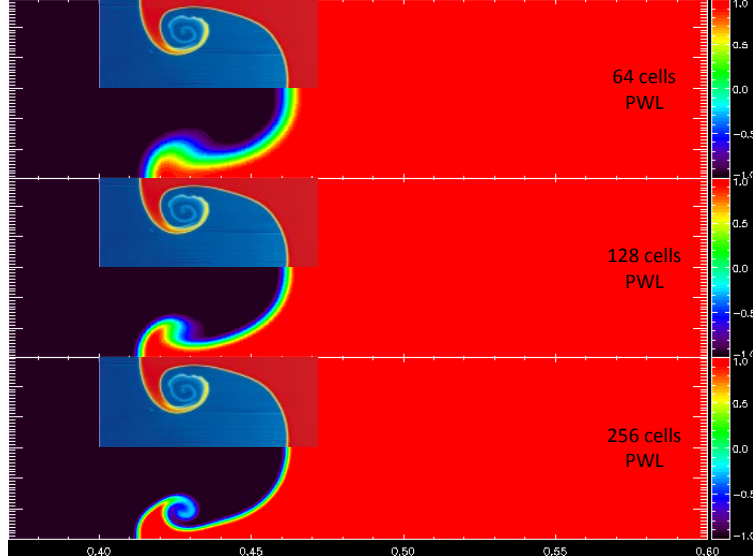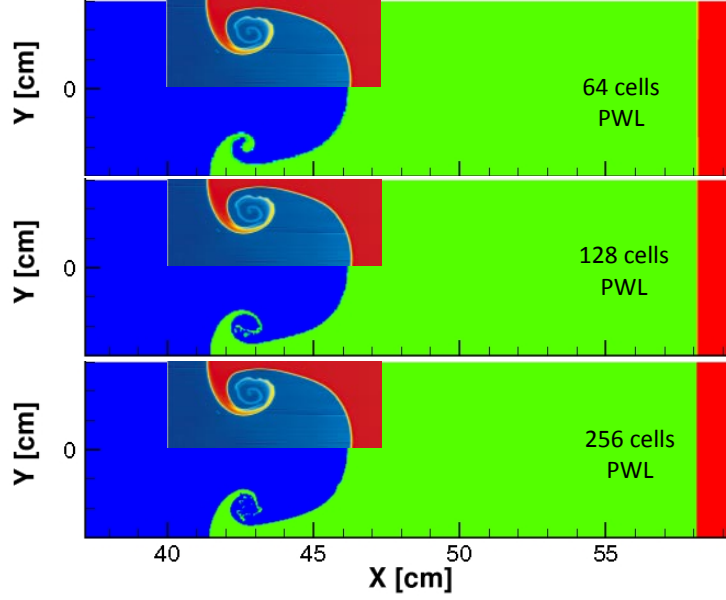
Figure 4.3: From top to bottom: density plot of the instability at $t = 6$ ms given by the DAFNA simulation with resolution = 64, 128, and 256 cells per wavelength respectively. The position along the x-axis is given by the unit of centimeters due to internal normalization. The insets are the PLIF image from the experiment [6] taken at $t = 6.006$ ms for comparison.

the turbulence and its energy cascade, as illustrated by Figure 4.4.

Overall, CRASH proves able to accurately model the linear growth phase of RTI and the experimentally observed RMI, given sufficient resolution. The necessary resolution is determined by the effect of numerical material diffusion, which is in turn determined by the speed of sound, size of the system, and the physical time of observation given the same numerical scheme and similar instabilities like RTI and RMI.
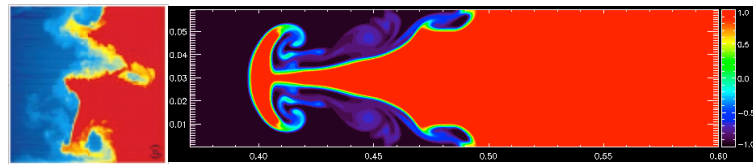
Figure 4.4: Left: PLIF image from the experiment at $t = 9.021$ ms [6] Right: SF_6 level set plot at $t = 9$ ms from the CRASH simulation with 256 cells per wavelength. Turbulence is deposited by the reflected shock at $t_{reshock} \sim$ 6.6 ms, a process not properly modeled by the simulations.
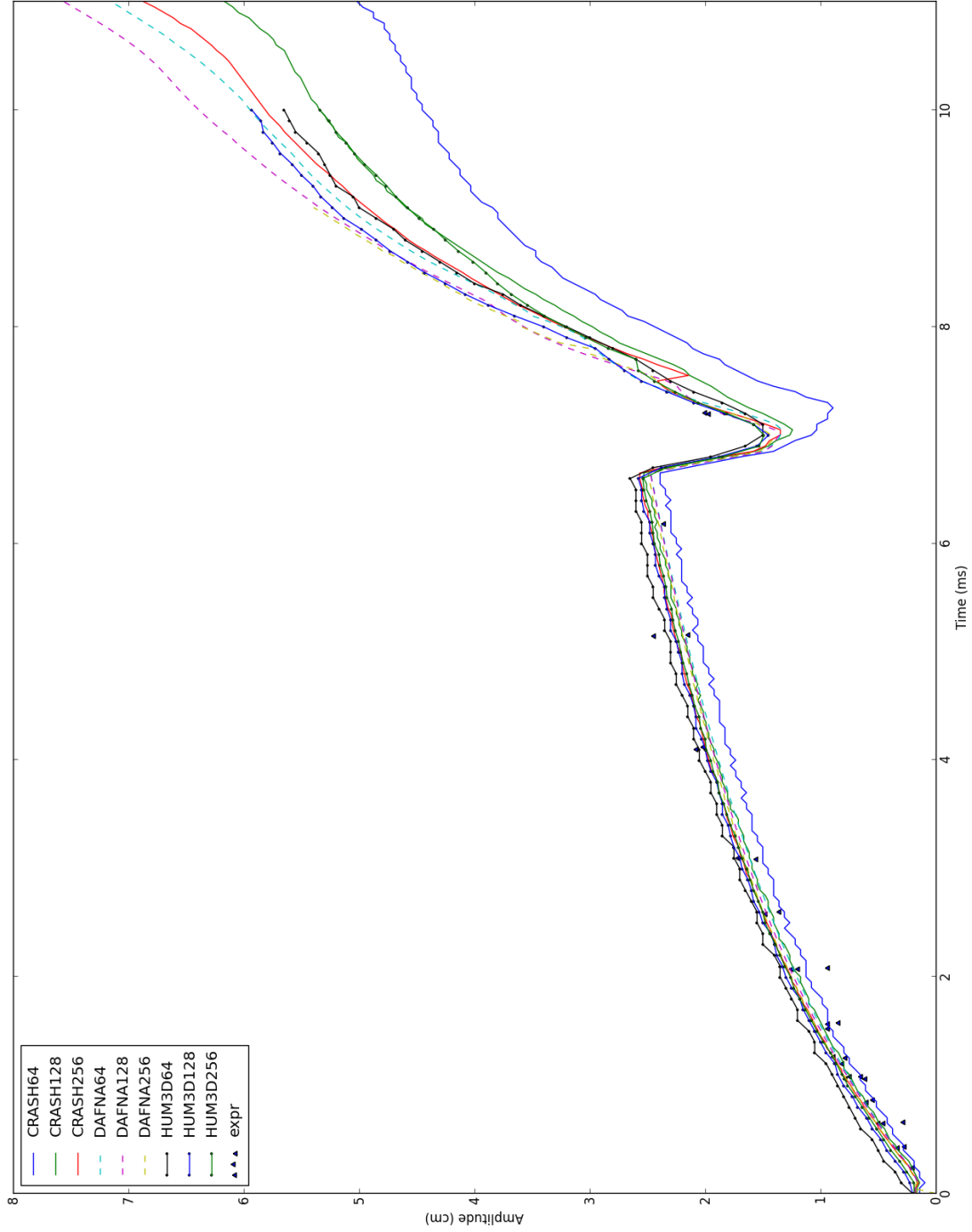
Figure 4.5: Instability amplitude over time given by CRASH, DAFNA, and HUM3D versus the data points given by the experiment [37]. The growth of the RMI is interrupted by the reflected shock at $t_{reshock} \sim 6.6$ ms.

CHAPTER V

CRASH Simulations of Rayleigh-Taylor Instability with Biermann Battery Effect

5.1   Introduction

Having shown that we can use CRASH to obtain reasonable results for both RTI and RMI simulations, we are finally ready to use CRASH's implementation of the Biermann battery term and magnetic diffusion term for the full SNRT simulations. We started with the relevant verification tests of the CRASH nightly test suite to test the Biermann battery implementation's behavior under semi-discontinuous initial conditions, and then performed the 2D/3D simulations of the SNRT instability with Biermann battery effect. We will conclude with a discussion of the discrepancy and limitations of the code.

5.2   Biermann Battery and Magnetic Diffusion Term with Continuous Setup

Both the Biermann battery term and the magnetic diffusion term due to resistivity are covered in the CRASH nightly test suit. For the Biermann battery test, the simulation domain is set up as a 2D 20×20 m box with periodic boundary condition

such that the electron pressure varies sinusoidally in the y-direction between $0.9 \sim 1.1$ Pa, and the density varies sinusoidally between $0.9 \sim 1.1$ kg/m^3 in the x-direction. The total pressure is kept constant at 2 Pa to keep the fluid stationary, and the electron number density n_e is artificially set to be proportional to the mass density ρ with the ratio $\rho/n_e \sim 1.7960634 \times 10^{-22}$ kg. Consequently, the generated $\mathbf{B}_z$ is antisymmetric with respect to both the central x-axis and y-axis and can be solved analytically with elementary functions. The test is set up with base grid resolutions 10×10, 20×20, and 40×40 cells for the whole simulation domain, but the 4×4 m square in the center is refined for one level (therefore contains 4×4, 8×8, and 16×16 cells instead, respectively) to make sure that the implementation doesn't break when adaptive mesh refinement (AMR) is on. All of these tests are run with CRASH's implementation of the HLLE scheme [15] and generalized Korens limiter [31] with $\beta = 1.5$ as described in Section 2.2.

Figure 5.1 shows the $\mathbf{B}_z$ calculated by the code and the error compared to the analytical solution. Although some noise is produced at the boundary of grid refinement, overall the calculated $\mathbf{B}_z$ converged to the analytical solution. In particular, first-order convergence is achieved for the maximum (L_∞ distance) error and second-order convergence is achieved for the L_1 distance between the calculated result and the analytical result after the first time step (Figure 5.2). The result at the final time step is more affected by the grid refinement boundary, but empirically the total relative error $\left(\sum |\mathbf{B}_{z,simulation} - \mathbf{B}_{z,analytic}| / \sum |\mathbf{B}_{z,analytic}| \right)$ converges with a rate that is between first and second order (Figure 5.3).

For the resistivity test, the simulation domain is similarly set up as a 2D 10×10 m box with periodic boundary condition and one level of grid refinement in the 2×2 m center square. The density, electron pressure, and total pressure are set to be constant at 1 kg/m^3, 1 Pa, and 2 Pa, respectively. $\mathbf{B}_x$ and $\mathbf{B}_z$ are set to vary sinusoidally in the y-direction (Figure 5.4) between ± 0.5 internal normalization unit,
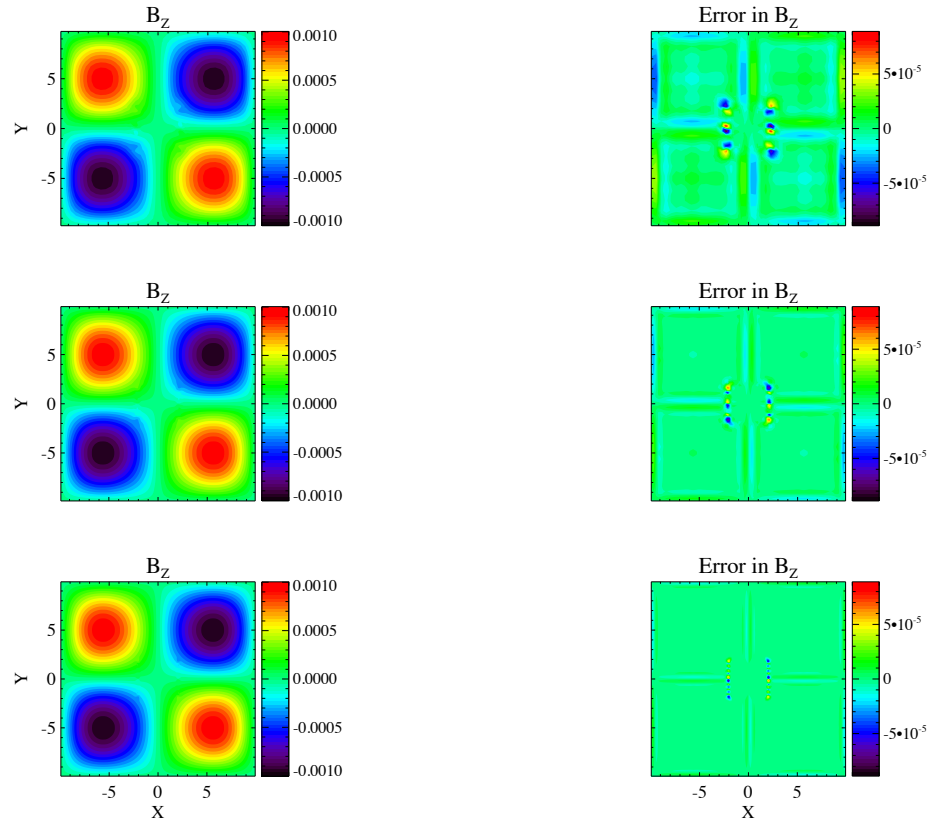
Figure 5.1: $\mathbf{B}_z$ calculated with increasing resolution from top to bottom and the error compared to the analytical solution for the Biermann battery test. The magnetic field is in CRASH code's internal normalization unit, which is ~ 0.00112 T here. Notice the noise at the refinement boundary.
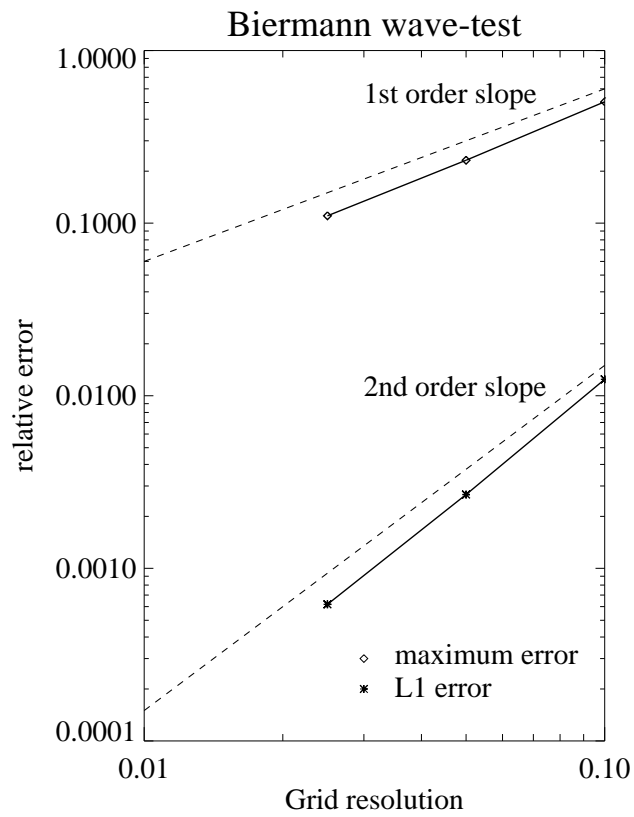
Figure 5.2: log-log graph of the point-wise relative error vs. grid resolution after the first time step for the Biermann battery test.
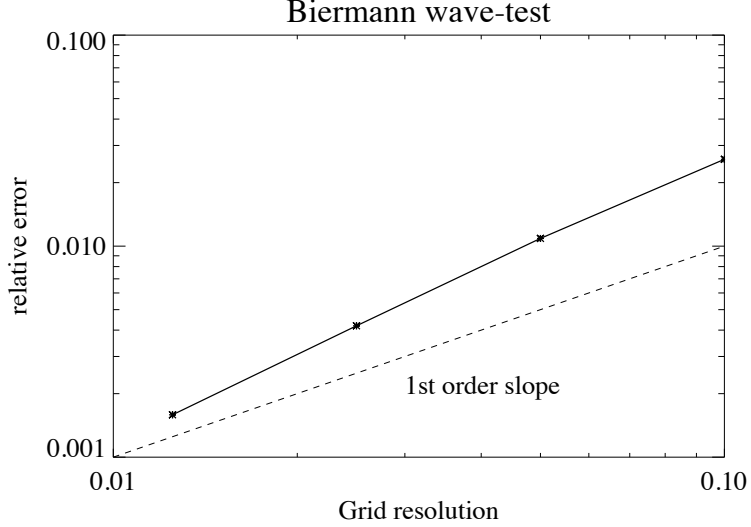
Figure 5.3: log-log graph of the total relative error $\left(\sum |\mathbf{B}_{z,simulation} - \mathbf{B}_{z,analytic}|/\sum |\mathbf{B}_{z,analytic}|\right)$ at the final time step for the Biermann battery test.

or $\sim 5.6 \times 10^{-4}$ T. With origin set at the center, the phases of $\mathbf{B}_x$ and $\mathbf{B}_z$ are offset by $90°$ such that $\mathbf{B}_x \propto \cos(ky)$ and $\mathbf{B}_z \propto -\sin(ky)$. The resistivity is set to be constant such that the magnetic diffusion constant $\eta = 1/\mu_0\sigma = 20$ m^2/s. In addition, the fluid in this test is given an initial velocity in the x-direction $u_x = 1$ m/s to test the effect of advection and induction. This test also includes the effect of Joule heating, and again runs with base grid resolutions 10×10, 20×20, and 40×40 cells with the HLLE scheme [15] and generalized Korens limiter [31] with $\beta = 1.5$. Point-wise second-order convergence is achieved for the L_1 distance from the analytical solution after the first time step (Figure 5.5).

5.3 Biermann Battery Term with Semi-continuous Setup

The expression for the Biermann battery term

$$\frac{\partial \mathbf{B}}{\partial t} = (k_B/e)(\nabla T_e \times \nabla \ln n_e) \tag{1.4}$$

breaks down in the presence of discontinuity, so quantitative validation isn't possible

Figure 5.4: $\mathbf{B}_x$, $\mathbf{B}_z$, electron pressure P_e due to Joule heating and the associated error with increasing resolution from left to right for the resistivity test. The noise at the refinement boundary vanishes as resolution increases.

Figure 5.5: log-log graph of the point-wise relative error (L_1 distance) vs. grid resolution after the first time step for the resistivity test.
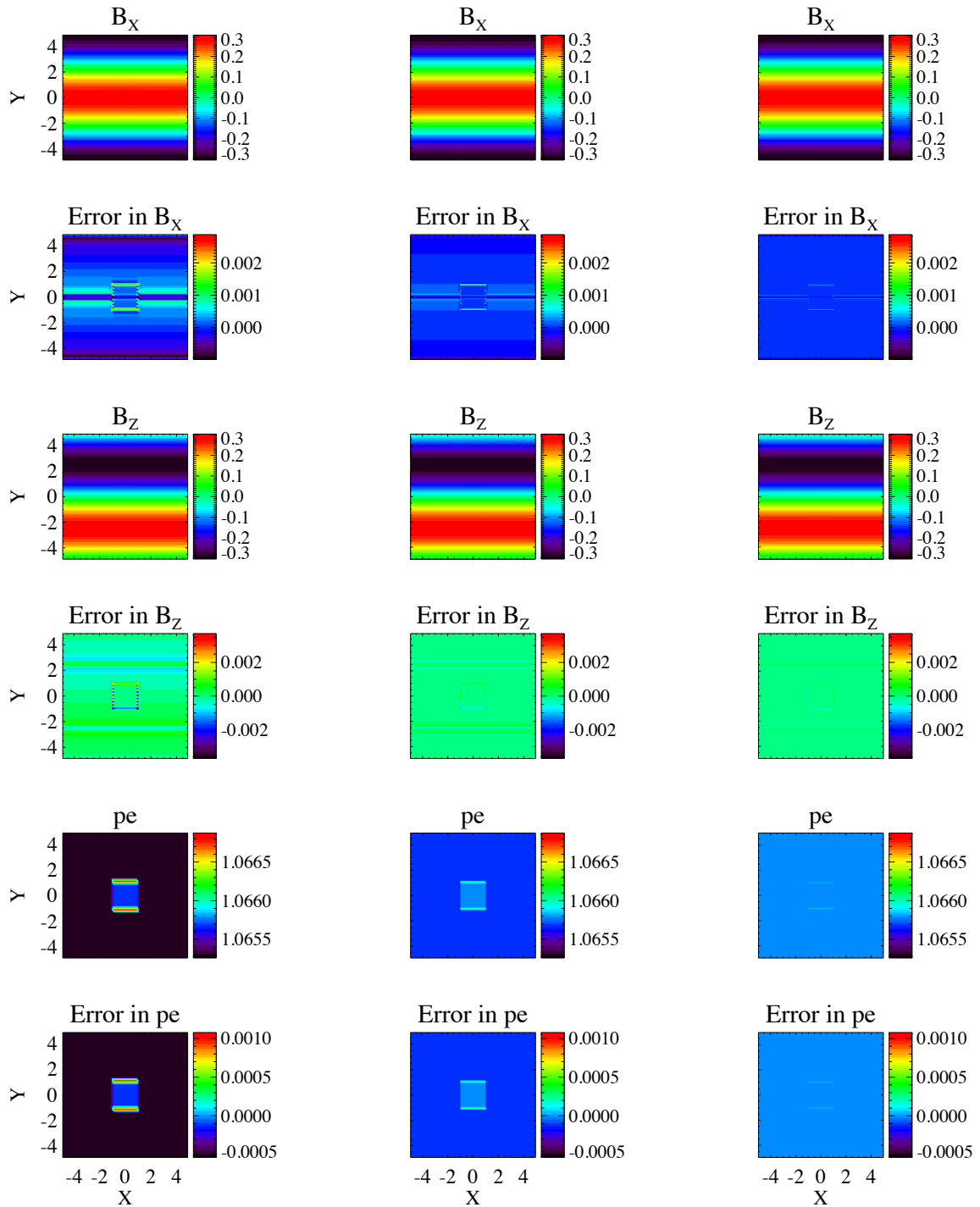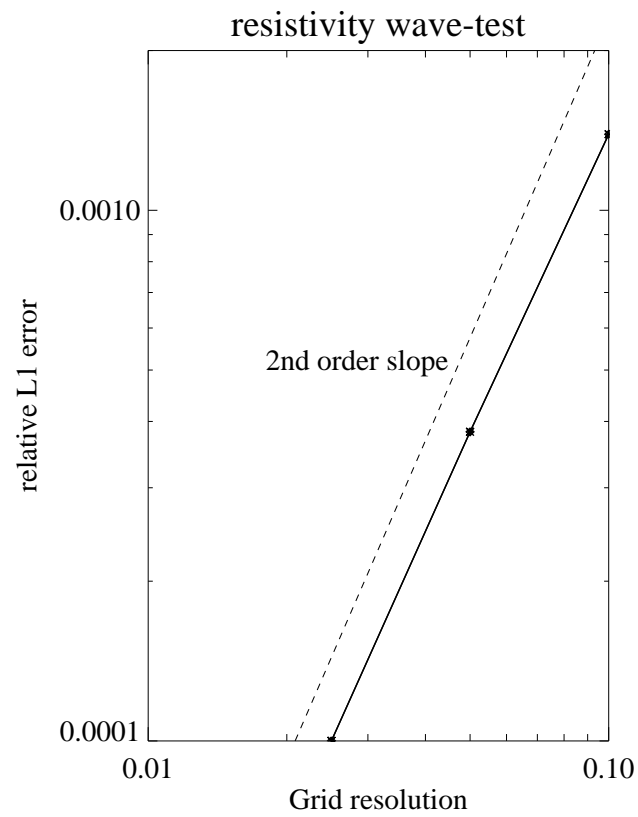
for a semi-continuous setup. However, since effective discontinuity at the length scale of typical grid resolution is ubiquitous for hydrodynamic and MHD simulations, we would like to ensure reasonable behavior in such case.

2D cylindrical geometry is used for this test, with periodic boundary condition in the axial direction and floating (outflow) boundary condition in the radial direction. The length and radius of the 2D simulation domain are 100 m and 25 m, respectively. The standard internal tabular EOS and opacity of Beryllium (Be) in the CRASH code is used for all of the fluid in this test, and the center column of the simulation domain (with radius $r = 7.5$ m) is set to have density varying sinusoidally between $2 \sim 4$ g/cc in the x-direction (Figure 5.6). T_e is set to be 80 eV when density is 3 g/cc, and varies to keep the pressure constant in the center column of the simulation domain. The rest of the simulation domain is set to have density 0.2 g/cc and $T_e = 200$ eV. Magnetic diffusion is turned off for this test, and the pressure jump between them is not expected to be relevant at the tested time scale. This test runs with resolutions 64×16, 128×32, 256×64, and 512×128 cells, with the standard CRASH heat conduction and multigroup diffusion for radiation transport.

The exact magnitude of the $\frac{\partial \mathbf{B}}{\partial t}$ is determined by the stencil of the implementation, but as we can see from Figure 5.7 the initial growth rate approximately doubles as we double the resolution as expected. Afterwards, the heat conduction model and inherent diffusion of the HLLE scheme take over and reduces the cross gradients and $\frac{\partial \mathbf{B}}{\partial t}$. Overall, the implementation of the Biermann battery term is both robust and accurate under applicable circumstances.

5.4   2D SNRT Simulation

With the relevant terms tested, we now turn to the original problem [34]. Due to the constraint of CPU flops and the explicit time integration of the resistivity term (explained in further detail in the next section), we focus mostly on a 2D version of
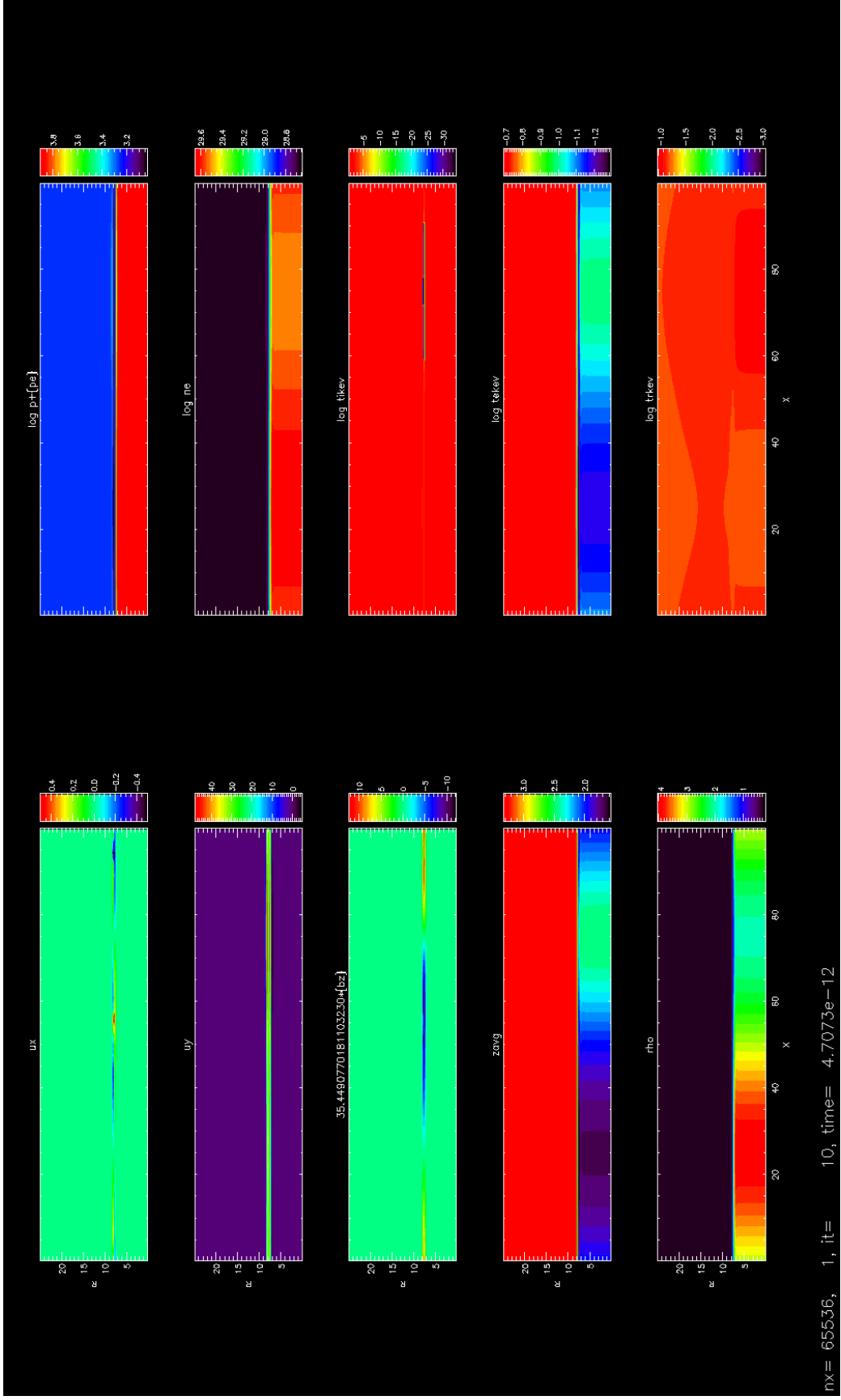
Figure 5.6: The final time step of the semi-discontinuous Biermann battery test at the highest resolution. $\mathbf{B}_\phi$ (internally marked as $\mathbf{B}_z$) is generated along the discontinuity and strongest along the maximum slope of the sinusoidally-varying density.
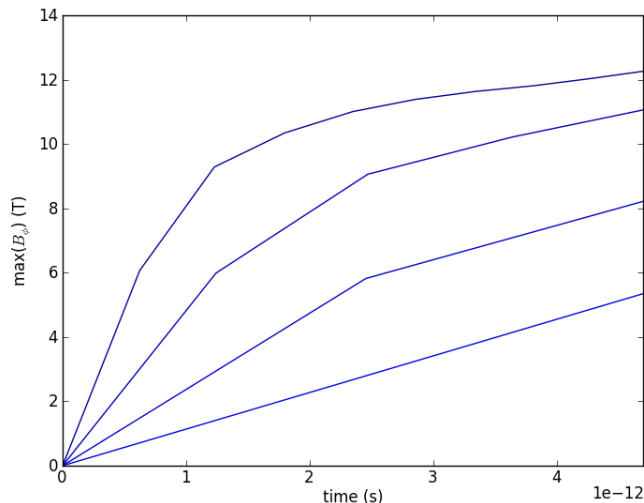
Figure 5.7: $\max(\mathbf{B}_\phi)$ over time for the semi-discontinuous Biermann battery test with doubling resolutions. Higher resolutions are indicated by darker blue.

the original experiment with cylindrical geometry. Most of the experimental setup is accurately modeled, except the necessitated change of the perturbation geometry from the original egg-crate pattern to a concentric, ripple-like pattern with the same wavelength $\lambda = 71$ μm and amplitude $a = 2.5$ μm. While the original Magnetic Straitjacket hypothesis cannot be tested against the morphology evolution of the concentric rings, we expect a spike placed in the center to evolve just like a single finger in the original 3D experiment given the similarity of geometry, and set the simulation up as such. In addition, the resulting gradients of T_e and n_e should also be applicable to the experimental condition.

The qualitative results are robust to variations, but we focus our analysis on the simulation of a specific SNRT experiment, shot 55295 in year 2009. The total laser energy of shot 55295 is 4.4704 KJ, and the laser beams have identical temporal power profile which can be described as a symmetric trapezoid: the power of the laser rises from zero to the maximum linearly from $t = 0$ to $t = 0.1$ ns, the maximum power is sustained from $t = 0.1$ ns to $t = 0.9$ ns, and the power falls from the maximum back to zero linearly from $t = 0.9$ ns to $t = 1.0$ ns. The axes of the laser beams are placed

# of beams	angle
2	10.32°
2	31.71°
3	42.28°
3	50.55°

Table 5.1: Numbers of laser beams at each angle relative to the shock tube axis for shot 55295 in year 2009

at an angle relative to the axis of the shock tube, and the numbers of beams at each angle are summarized in Table 5.1. On the other hand, the azimuthal angles of the laser beams are ignored in the simulation due to the inherent limitation of the 2D cylindrical geometry.

The axes of the laser beams go through the origin, which is the center of the surface of the polyimide disk facing outward. The power of each laser beam was approximately equal in the experiment and is set to be equal in the simulation for simplicity. The spatial irradiance profile of the laser beams is super-Gaussian of order 4.2, that is, the irradiance I of the beam at distance r from the axis is proportional to $e^{-(r/rBeam)^{4.2}}$. $rBeam$ can be considered to be the radius of the beams and is equal to 410 μm in this case. CRF foam is modeled as low-density carbon, and polyimide plasma is modeled as a mixture of four elements according to the chemical formula $C_{22}H_{10}O_5N_2$. The EOS table and opacity table are then generated by PROPACEOS from PRISM Computational Sciences, Inc. and converted to the format used by CRASH. The CHBr tracer strip is not modeled separately from the polyimide disk since we do not expect it to affect the dynamics significantly [4]. Radiation transport is modeled as multigroup diffusion, although we do not expect the shock to be significantly radiative in this case. The size of each cell is 3.375×3.5 μm for the base grid. Right at the material interface after two levels of AMR, the size of the smallest cells is 0.84375×0.875 μm.

Figure 5.8 shows the final state of the simulation 21 ns after the firing of the laser, and Figure 5.9 zooms in on the density profile of the unstable region. At
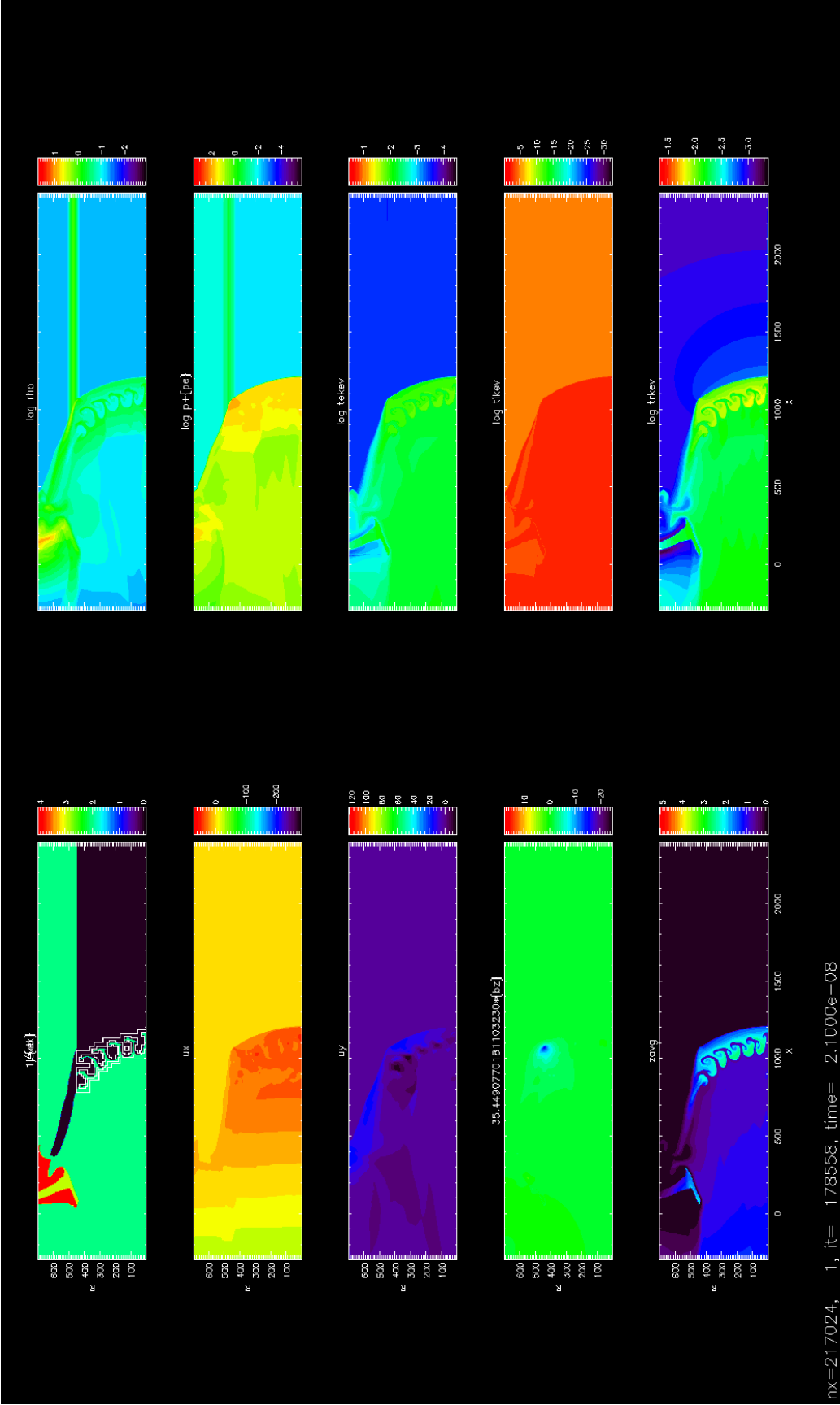
Figure 5.8: 2D SNRT simulation at $t = 21$ ns. Length unit in μm. Left column: level-set and refinement boundary, velocity along the axis (km/s), radial velocity (km/s), $\mathbf{B}_\phi$ (Tesla, marked as $\sim 35.45 \times \mathbf{B}_z$ due to internal normalization), and average ionization $\bar{Z}$. Right column: logarithm of density (g/cm^3) log ρ, logarithm of total pressure (10^9 pascal) log p, logarithm of electron temperature (keV) log T_e, logarithm of ion temperature (keV) log T_i, and logarithm of radiation temperature (keV) log T_r.

such late time, the most prominent magnetic field we observed is generated from the near-vertical angle between the shock and the material interface near the tube wall, although such effect may not be fully physical since this material interface along the tube wall is effectively a contact discontinuity. Examination at early time shows that the dominant magnetic field is generated along the shock front, especially when the shock hits the perturbation (Figure 5.10). This pattern of $\mathbf{B}_\phi$ can be explained by considering the tangential gradients of T_e and n_e along the shock front. The strength of the shock is approximately uniform near the axis of the shock tube due to the shape of the laser beams. Therefore the gradients vanish and no magnetic field is generated until the shock hits the perturbation. The small but significant difference in shock strength due to the interface perturbation persists afterward and continues to generate nonzero $\mathbf{B}_\phi$, as we can see in Figure 5.11. In comparison, the magnetic field generated along the material interface is much weaker in magnitude since the T_e gradient and n_e gradient are mostly aligned and anti-parallel to each other (Figure 5.11). The magnitude of the magnetic field at the location relevant to the Magnetic StraightJacket hypothesis $|\mathbf{B}_\phi|$ tops out ~ 1 T (Figure 5.12) at 7 ns, but stays below 0.6 T most of the time for the rest of the simulation. Based on the T_e, n_e, and $\bar{Z}$ we get from the simulation and Spitzer conductivity, the magnetic diffusion constant $\eta = 1/\mu_0\sigma$ is estimated to be ~ 4 m^2/s at 7 ns posteriorly. However, the magnetic diffusion constant is fixed at 0.9076 m^2/s throughout the simulation priorly in order to maintain reasonable size of the time step, so the experimental condition is likely to be more unfavorable towards sustaining magnetic field. However, the resistivity and diffusion rate both decrease strongly as temperature increases, and the resistive heating rate is of the same order as the diffusion rate. Unfortunately, the calculations we were able to do proved unable to address the interplay between diffusion and heating.
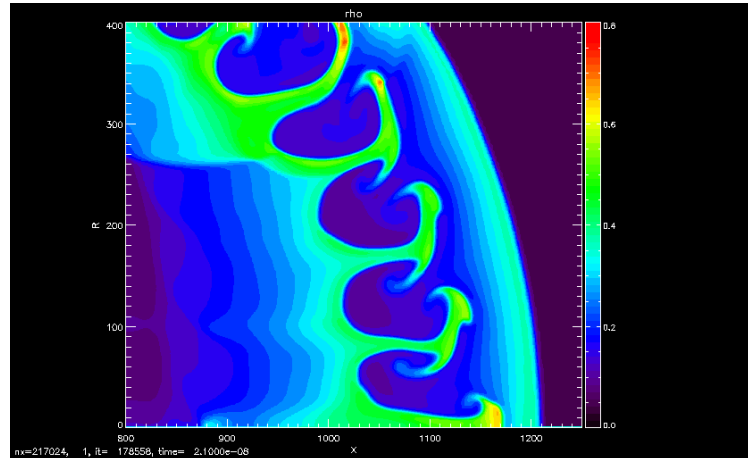
Figure 5.9: Density (g/cm^3) profile zoom-in on the instability at 21 ns. A mushroom cap is present on the center spike but not as prominent as in the FLASH simulation in Figure 1.8.
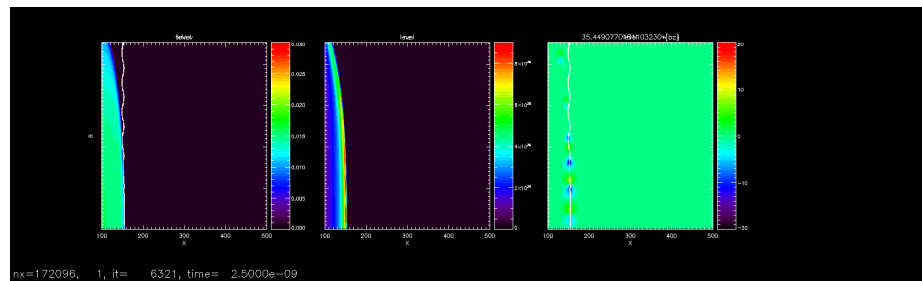
Figure 5.10: Electron temperature T_e (keV), electron number density (m^{-3}), and magnetic field $\mathbf{B}_\phi$ (Tesla) at 2.5 ns with material interface marked as white contour. Strong magnetic field is generated where shock hits the perturbation.
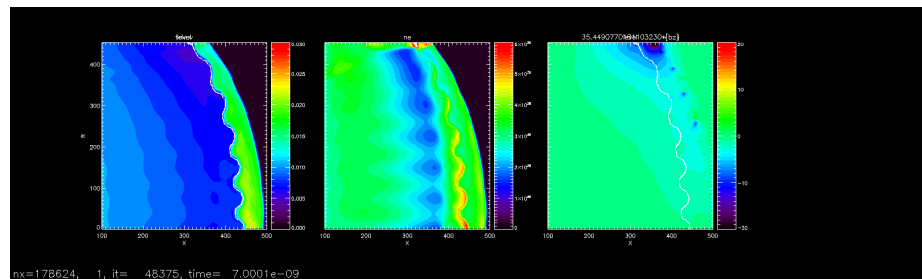
Figure 5.11: Electron temperature T_e (keV), electron number density n_e (m^{-3}), and magnetic field $\mathbf{B}_\phi$ (Tesla) at 7 ns. A stronger magnetic field is generated along the rippled shock front than at the material interface. Note that scale is adjusted and the redundant contour is taken out for n_e.
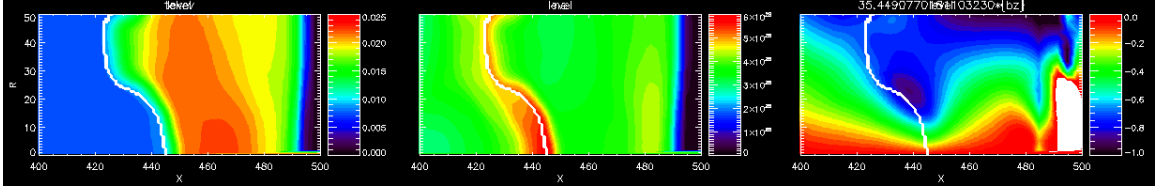
Figure 5.12: Electron temperature T_e (keV), electron number density n_e (m^{-3}), and magnetic field $\mathbf{B}_\phi$ (Tesla) at 7 ns along the material interface, with scale adjusted for the magnetic field at the relevant location.

5.5 3D SNRT Simulation

Finally, we attempted a 3D version of the simulation. Due to the limitation of the laser package and CPU time, we restricted the problem to 1/8 of the wavelength of the center spike with reflective boundary condition in the y- and z-direction, and used the laser heating data from the corresponding 2D simulation to initialize the 3D simulation. However, we encountered some stability issues and were therefore forced to set an even higher magnetic diffusion constant at 2.269 m^2/s. Since the time integration of the magnetic diffusion is implemented explicitly, the time step is limited at $\Delta t \sim \Delta x^2 / \mathrm{D}_{magnetic}$. When we hit the scaling limit of the code with one core handling one $6 \times 6 \times 6$ block, we were only able to complete the simulation with the resolution of 48 cells per wavelength within reasonable time. The result is consistent with the 2D result, although we cannot draw further conclusions from it (Figure 5.13).

5.6 Conclusion and Discussion

Given the strength of the magnetic field, we do not expect it to play a significant role in the dynamics of the system for the 2D/3D SNRT simulations. Indeed, the CRASH simulation without the Biermann battery effect results in indistinguishable spike morphology (Figure 5.14) and quantitatively reproduces near-identical insta-
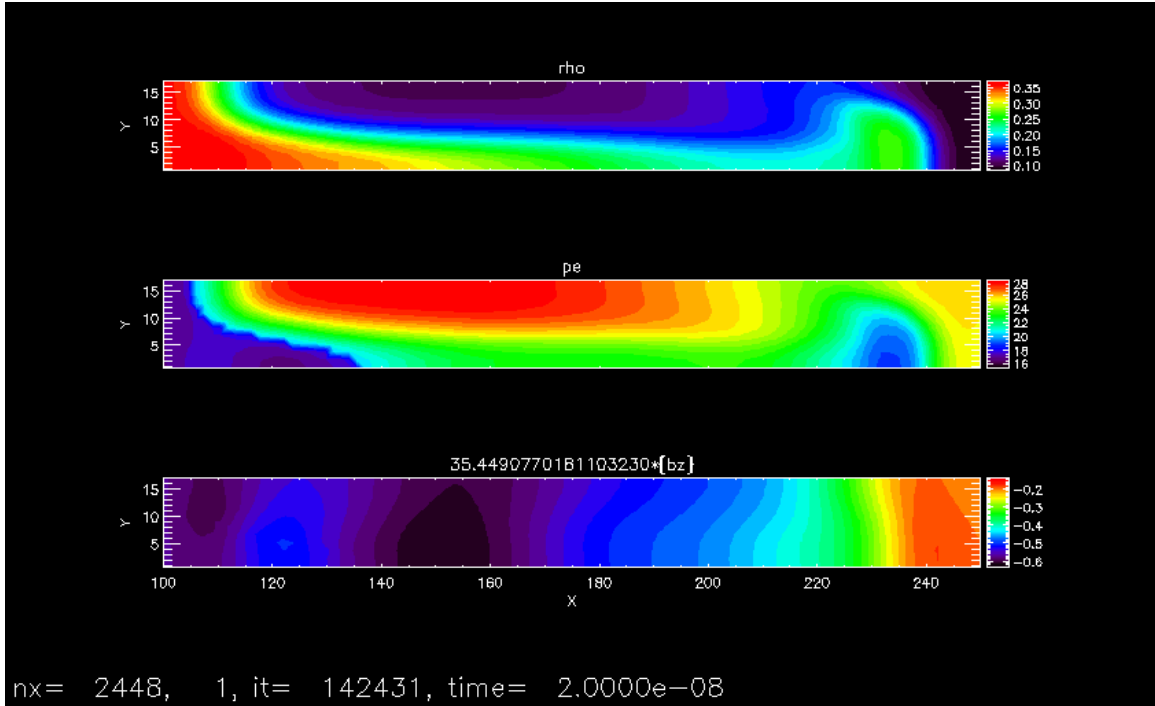
Figure 5.13: "Center spike" of the 3D SNRT simulation, as part of the conceptually infinite sheet of spikes and bubbles at 20 ns: density (g/cm^3) ρ, electron pressure p_e (10^9 pascal), and magnetic field in the direction perpendicular to the plane $\mathbf{B}_z$ (Tesla). The x-position does't correspond to the x-position of the 2D simulation since a simple Galilean transformation is applied to keep the instability in the simulation domain.
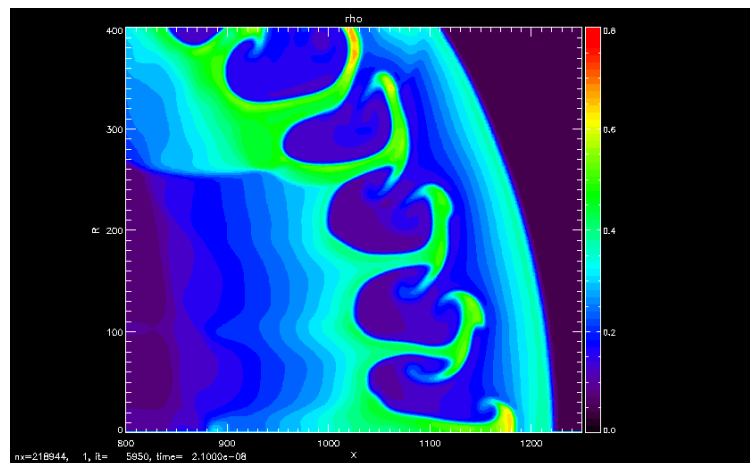
Figure 5.14: Density (g/cm^3) profile zoom-in on the instability at 21 ns for the 2D SNRT CRASH Simulation without the Biermann battery effect. The morphology is indistinguishable from Figure 5.9.
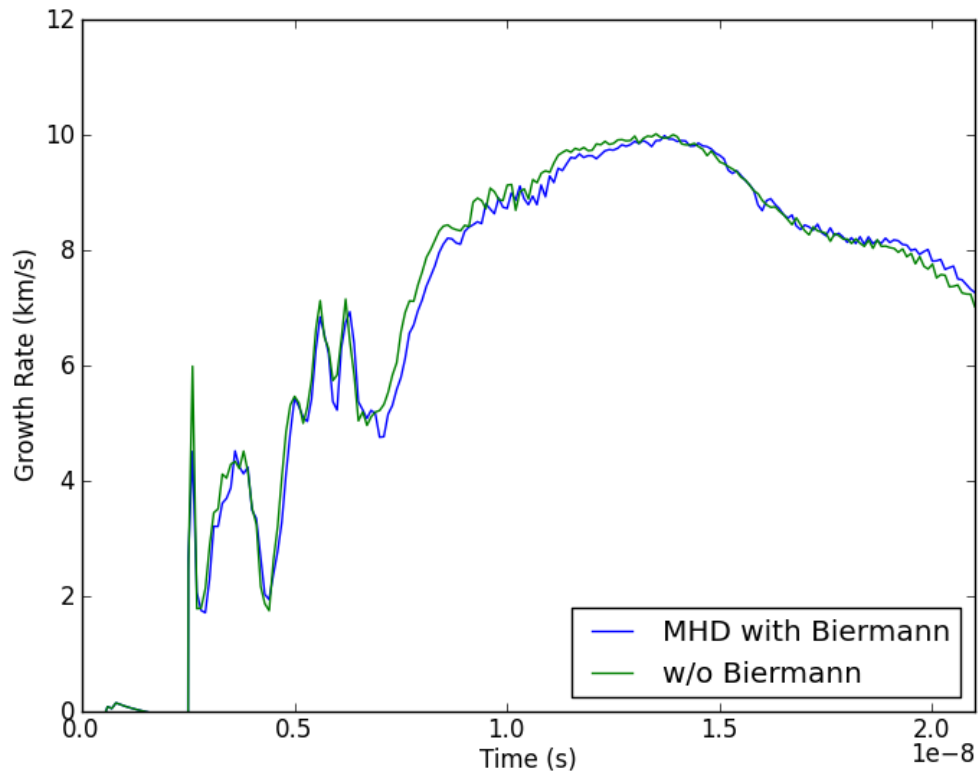
Figure 5.15: Growth rate of the instability for the 2D SNRT simulations, with and without the Biermann battery effect. The growth rate is measured by the relative horizontal velocity between the tip of the center spike and the tip of the surrounding bubble.

bility growth rate (Figure 5.15). Therefore, it is tempting to rule out the Magnetic Straightjacket hypothesis based on the result, especially given the underestimation of the resistivity. Unfortunately, these Eulerian simulations turn out to be under-resolved. Based on the T_e, n_e, $\bar{Z}$, and ρ we get from the simulation at 7 ns, the heat diffusion constant is estimated to be $\chi \sim 4$ $(cm^2\ s^{-1})$ for the carbon foam bubble and ~ 0.76 $(cm^2\ s^{-1})$ for the polyimide spike using Equation 2.6. Consequently, on the timescale of $4 \sim 18$ ns after the shock hit the interface, the temperature jump should only diffuse across $1 \sim 2$ μm physically. Since Eulerian codes like CRASH numerically require $4 \sim 5$ cells to resolve such interface, the dimension of the cells at the interface has to be ≤ 0.2 μm in order to fully resolve the temperature gradient. It takes at least the same resolution to fully resolve the gradient of $\ln n_e$ due to its dependence on temperature. Electron number density n_e also depends on the identity of the material, which is determined by the level set method without mixed cells in these CRASH simulations. The identity of the material therefore does not require higher resolution to resolve, but the level set method may have other complications like spurious oscillations. If we assume that the gradients of electron temperature and number density are inversely proportional to the size of the cell until the simulation is well-resolved, the magnetic field could be 16 times as large, with corresponding magnetic pressure that stays below 3.7×10^7 Pa most of the time but occasionally reaches 10^8 Pa. While still small relative to the total pressure experienced by the spikes ($\sim 10^{11}$ Pa), it may nonetheless be sufficient to prevent the lateral development of KHI. In fact, magnetic pressure that is $\sim 1/2500$ of the total pressure has been shown to be sufficient [18]. Realistic simulation with sufficient resolution, however, is certainly beyond the current capacity of CRASH and available CPUs. The time step limit due to the explicit time integration of the magnetic diffusion $\Delta t \sim \Delta x^2/D_{magnetic}$ dictates that sufficient resolution and physically realistic magnetic diffusion constant would require at least a 64-fold increase of the count of total floating point operations, therefore more
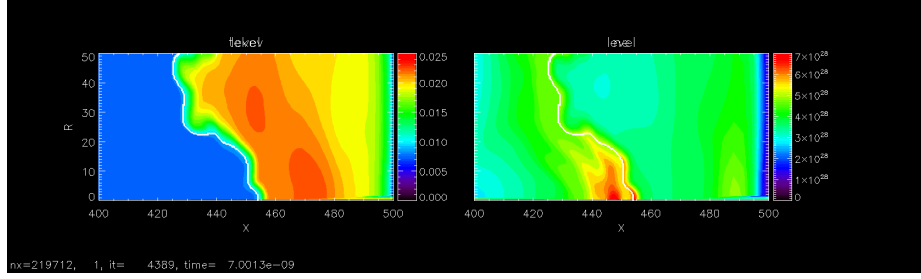
Figure 5.16: Electron temperature T_e (keV) and electron number density n_e (m^{-3}) at 7 ns from the 2D SNRT CRASH Simulation with one more level of AMR but no Biermann battery effect. Secondary small-wavelength instabilities are already prominent when the smallest cells are of the dimension 0.421875×0.4375 μm.

than a year on 200 cores instead of 8 days on the available hardware. To complicate the issue further, a pilot run with pure hydrodynamics and one more level of AMR shows that HLLE scheme will generate secondary small-wavelength instabilities along the interface, once the temperature gradient is fully resolved (Figure 5.16). If these small-wavelength instabilities are not adequately suppressed by the magnetic field lines normal to them, generated by the Biermann battery effect in the corresponding high-resolution MHD run, we will not be able to simulate the evolution of the morphologies of the SNRT instability realistically with the current numerical scheme, even with sufficient computational resources.

CHAPTER VI

Conclusions and Future Directions

In the previous chapters, we can see that CRASH is capable of modeling both RTI and RMI, given the appropriate choice of numerical scheme, flux limiter, and resolution. We have also tested its implementation of Biermann battery and magnetic diffusion. Taken together, however, CRASH is not capable of simulating the SNRT system with Biermann battery effect, with the physical realism necessary to support or refute the Magnetic Straightjacket hypothesis conclusively.

Knowing what the code cannot do, however, is as important as knowing what the code can do. The explicit time integration of the magnetic diffusion is a known limitation for the time step size, and effort is underway to implement the implicit time integration for the magnetic diffusion. The growth of secondary small-wavelength instabilities, however, may prove to be a more fundamental challenge. Since the Biermann battery term is proportional to the gradients in electron temperature T_e and logarithm of electron number density $\ln n_e$, we need to fully resolve the interface. At the same time, small-wavelength instabilities tend to grow in simulations with high resolution and low numerical material diffusion, as we can see in the pilot runs of Chapter V and Chapter III. Implementation of another numerical scheme or development of a new numerical scheme may therefore be necessary to model the full SNRT system with Biermann battery effect, as such multidimensional RT-unstable systems

turn out to be a more difficult challenge for Eulerian codes than anticipated, once coupled to a gradient-dependent term like Biermann battery. What we can say is that we have uncovered additional criteria for such simulations, waiting future iterations of CRASH or other code packages to fulfill.

BIBLIOGRAPHY

BIBLIOGRAPHY

[1] J. E. Bailey, G. A. Rochau, R. C. Mancini, C. A. Iglesias, J. J. MacFarlane, I. E. Golovkin, C. Blancard, Ph. Cosse, and G. Faussurier. Experimental investigation of opacity models for stellar interior, inertial fusion, and high energy density plasmas. *Physics of Plasmas*, 16(5):058101, 2009.

[2] L. Biermann. *Zs. Naturforschung., 5a*, pages 65–71, 1950. cited By (since 1996) 1.

[3] Jay P. Boris. A fluid transport algorithm that works. In *Computing as a language of physics*, pages 171–189. International Atomic Energy Agency, 1971.

[4] A. Budde, R.P. Drake, C.C. Kuranz, M.J. Grosskopf, T. Plewa, and N.C. Hearn. Simulation of fabrication variations in supernova hydrodynamics experiments. *High Energy Density Physics*, 6(2):135 – 142, 2010. ICHED 2009 - 2nd International Conference on High Energy Density Physics.

[5] C.-C. Chou, B. Fryxell, and R.P. Drake. Rayleigh-Taylor instability simulations with CRASH. *High Energy Density Physics*, 8(1):71 – 75, 2012.

[6] B. D. Collins and J. W. Jacobs. PLIF flow visualization and measurements of the richtmyer-meshkov instability of an air/sf6 interface. *Journal of Fluid Mechanics*, 464:113–136, 2002.

[7] H Costantini, A Formicola, G Imbriani, M Junker, C Rolfs, and F Strieder. Luna: a laboratory for underground nuclear astrophysics. *Reports on Progress in Physics*, 72(8):086301, 2009.

[8] R. Courant, K. Friedrichs, and H. Lewy. Über die partiellen Differenzengleichungen der mathematischen Physik. *Mathematische Annalen*, 100:32–74, 1928.

[9] Guy Dimonte and P. Ramaprabhu. Simulations and model of the nonlinear richtmyer–meshkov instability. *Physics of Fluids*, 22(1):014104, 2010.

[10] F. W. Doss, H. F. Robey, R. P. Drake, and C. C. Kuranz. Wall shocks in high-energy-density shock tube experiments. *Physics of Plasmas*, 16(11):112705, 2009.

[11] R. P. Drake, H. F. Robey, O. A. Hurricane, Y. Zhang, B. A. Remington, J. Knauer, J. Glimm, D. Arnett, J. O. Kane, K. S. Budil, and J. Grove. Experiments to produce a hydrodynamically unstable, spherically diverging system of

relevance to instabilities in supernovae. *The Astrophysical Journal*, 564(2):896, 2002.

[12] R.P. Drake. *High-Energy-Density Physics: Fundamentals, Inertial Fusion, and Experimental Astrophysics*. Shock Wave and High Pressure Phenomena. Springer, 2007.

[13] S. Dürr, Z. Fodor, J. Frison, C. Hoelbling, R. Hoffmann, S. D. Katz, S. Krieg, T. Kurth, L. Lellouch, T. Lippert, K. K. Szabo, and G. Vulvert. Ab initio determination of light hadron masses. *Science*, 322(5905):1224–1227, 2008.

[14] J. S. Edwards and B. O. Palsson. The escherichia coli mg1655 in silico metabolic genotype: Its definition, characteristics, and capabilities. *Proceedings of the National Academy of Sciences*, 97(10):5528–5533, 2000.

[15] B. Einfeldt, C. D. Munz, P. L. Roe, and B. Sjgreen. On godunov-type methods near low densities. *Journal of Computational Physics*, 92(2):273 – 295, 1991.

[16] J. M. Foster, B. H. Wilde, P. A. Rosen, R. J. R. Williams, B. E. Blue, R. F. Coker, R. P. Drake, A. Frank, P. A. Keiter, A. M. Khokhlov, J. P. Knauer, and T. S. Perry. High-energy-density laboratory astrophysics studies of jets and bow shocks. *The Astrophysical Journal Letters*, 634(1):L77, 2005.

[17] Gary Fraley. Rayleigh–taylor stability for a normal shock wave–density discontinuity interaction. *Physics of Fluids*, 29(2):376–386, 1986.

[18] B. Fryxell, C.C. Kuranz, R.P. Drake, M.J. Grosskopf, A. Budde, T. Plewa, N. Hearn, J.F. Hansen, A.R. Miles, and J. Knauer. The possible effects of magnetic fields on laser experiments of rayleigh-taylor instabilities. *High Energy Density Physics*, 6(2):162 – 165, 2010. ICHED 2009 - 2nd International Conference on High Energy Density Physics.

[19] S. K. Godunov. A difference scheme for numerical computation of discontinuous solution of hyperbolic equation. *Math. Sbornik*, 47:271 306, 1959.

[20] J Guzman and T Plewa. Non-spherical core-collapse supernovae: evolution towards homologous expansion. *Nonlinearity*, 22(11):2775, 2009.

[21] Eric C. Harding. *Observations of Shear Flows in High-Energy-Density Plasmas*. PhD thesis, University of Michigan, 2010.

[22] James Paul Holloway, Derek Bingham, Chuan-Chih Chou, Forrest Doss, R. Paul Drake, Bruce Fryxell, Michael Grosskopf, Bart van der Holst, Bani K. Mallick, Ryan McClarren, Ashin Mukherjee, Vijay Nair, Kenneth G. Powell, D. Ryu, Igor Sokolov, Gábor Tóth, and Zhanyang Zhang. Predictive modeling of a radiative shock system. *Reliability Engineering & System Safety*, 96(9):1184 – 1193, 2011. Quantification of Margins and Uncertainties.

[23] Richard L. Holmes, Guy Dimonte, Bruce Fryxell, Michael L. Gittings, John W. Grove, Marilyn Schneider, David H. Sharp, Alexander L. Velikovich, Robert P. Weaver, and Qiang Zhang. Richtmyer-meshkov instability growth: experiment, simulation and theory. *Journal of Fluid Mechanics*, 389:55–79, 1999.

[24] Morten Ø. Jensen, Vishwanath Jogini, David W. Borhani, Abba E. Leffler, Ron O. Dror, and David E. Shaw. Mechanism of voltage gating in potassium channels. *Science*, 336(6078):229–233, 2012.

[25] J. Kane, D. Arnett, B. A. Remington, S. G. Glendinning, G. Bazan, R. P. Drake, and B. A. Fryxell. Supernova experiments on the nova laser. *The Astrophysical Journal Supplement Series*, 127(2):365, 2000.

[26] J. Kane, D. Arnett, B. A. Remington, S. G. Glendinning, G. Bazan, R. P. Drake, B. A. Fryxell, R. Teyssier, and K. Moore. Scaling supernova hydrodynamics to the laboratory. *Physics of Plasmas*, 6(5):2065–2071, 1999.

[27] J. Kane, D. Arnett, B. A. Remington, S. G. Glendinning, J. Castor, R. Wallace, A. Rubenchik, and B. A. Fryxell. Supernova-relevant hydrodynamic instability experiments on the nova laser. *The Astrophysical Journal Letters*, 478(2):L75, 1997.

[28] J. O. Kane, H. F. Robey, B. A. Remington, R. P. Drake, J. Knauer, D. D. Ryutov, H. Louis, R. Teyssier, O. Hurricane, D. Arnett, R. Rosner, and A. Calder. Interface imprinting by a rippled shock using an intense laser. *Phys. Rev. E*, 63:055401, Apr 2001.

[29] Richard I. Klein, Kimberly S. Budil, Theodore S. Perry, and David R. Bach. The interaction of supernova remnants with interstellar clouds: Experiments on the nova laser. *The Astrophysical Journal*, 583(1):245, 2003.

[30] V.P. Kolgan. Application of the principle of minimizing the derivative to the construction of finite-difference schemes for computing discontinuous solutions of gas dynamics. *Journal of Computational Physics*, 230(7):2384 – 2390, 2011.

[31] B. Koren. *Numerical Methods for Advection-Diffusion Problems*, chapter A robust upwind discretization method for advection, diffusion and source terms, pages 117–138. Friedrich Vieweg & Sohn Verlag, 1993.

[32] R. M. J. Kramer, D. I. Pullin, D. I. Meiron, and C. Pantano. Shock-resolved navier-stokes simulation of the richtmyer-meshkov instability start-up at a light-heavy interface. *Journal of Fluid Mechanics*, 642:421–443, 2010.

[33] C. Kuranz, R. Drake, D. Leibrandt, E. Harding, H. Robey, A. Miles, B. Blue, J. Hansen, H. Louis, M. Bono, J. Knauer, D. Arnett, and C. Meakin. Progress toward the study of laboratory scale, astrophysically relevant, turbulent plasmas. *Astrophysics and Space Science*, 298(1-2):9–16, June 2005.

[34] C. C. Kuranz, R. P. Drake, M. J. Grosskopf, B. Fryxell, A. Budde, J. F. Hansen, A. R. Miles, T. Plewa, N. Hearn, and J. Knauer. Spike morphology in blast-wave-driven instability experiments. *Physics of Plasmas*, 17(5):052709, 2010.

[35] C. C. Kuranz, R. P. Drake, E. C. Harding, M. J. Grosskopf, H. F. Robey, B. A. Remington, M. J. Edwards, A. R. Miles, T. S. Perry, B. E. Blue, T. Plewa, N. C. Hearn, J. P. Knauer, D. Arnett, and D. R. Leibrandt. Two-dimensional blast-wave-driven rayleigh-taylor instability: Experiment and simulation. *The Astrophysical Journal*, 696(1):749, 2009.

[36] Carolyn C. Kuranz. *Blast-Wave-Driven, Multidimensional Rayleigh-Taylor Instability Experiments*. PhD thesis, University of Michigan, 2009.

[37] Marco Latini, Oleg Schilling, and Wai Sun Don. Effects of weno flux reconstruction order and spatial resolution on reshocked two-dimensional richtmyermeshkov instability. *Journal of Computational Physics*, 221(2):805 – 836, 2007.

[38] C. C. Long, V. V. Krivets, J. A. Greenough, and J. W. Jacobs. Shock tube experiments and numerical simulation of the single-mode, three-dimensional richtmyer–meshkov instability. *Physics of Fluids*, 21(11):114104, 2009.

[39] G Malamud, C A Di Stefano, Y Elbaz, C M Huntington, C C Kuranz, P A Keiter, and R P Drake. A design of a two-dimensional, multimode rm experiment on omega-ep. *HEDP*, under revision for publication.

[40] M. J.-E. Manuel, C. K. Li, F. H. Séguin, J. Frenje, D. T. Casey, R. D. Petrasso, S. X. Hu, R. Betti, J. D. Hager, D. D. Meyerhofer, and V. A. Smalyuk. First measurements of rayleigh-taylor-induced magnetic fields in laser-produced plasmas. *Phys. Rev. Lett.*, 108:255006, Jun 2012.

[41] Ryan G. McClarren, D. Ryu, R. Paul Drake, Michael Grosskopf, Derek Bingham, Chuan-Chih Chou, Bruce Fryxell, Bart van der Holst, James Paul Holloway, Carolyn C. Kuranz, Bani Mallick, Erica Rutter, and Ben R. Torralva. A physics informed emulator for laser-driven radiating shock simulations. *Reliability Engineering & System Safety*, 96(9):1194 – 1207, 2011. Quantification of Margins and Uncertainties.

[42] J.E. Morel. Diffusion-limit asymptotics of the transport equation, the p1/3 equations, and two flux-limited diffusion theories. *Journal of Quantitative Spectroscopy and Radiative Transfer*, 65(5):769 – 778, 2000.

[43] P. Movahed and E. Johnsen. A solution-adaptive method for efficient compressible multifluid simulations, with application to the richtmyer-meshkov instability. Submitted.

[44] David Pollard and Robert M. DeConto. Modelling west antarctic ice sheet growth and collapse through the past five million years. *Nature*, 458(7236):329–332, 03 2009.

[45] B. A. Remington, J. Kane, R. P. Drake, S. G. Glendinning, K. Estabrook, R. London, J. Castor, R. J. Wallace, D. Arnett, E. Liang, R. McCray, A. Rubenchik, and B. Fryxell. Supernova hydrodynamics experiments on the nova laser. *Physics of Plasmas*, 4(5):1994–2003, 1997.

[46] L. F. Richardson. The approximate arithmetical solution by finite differences of physical problems involving differential equations, with an application to the stresses in a masonry dam. *Philosophical Transactions of the Royal Society of London. Series A, Containing Papers of a Mathematical or Physical Character*, 210:pp. 307–357, 1911.

[47] Robert D. Richtmyer. Taylor instability in shock acceleration of compressible fluids. *Communications on Pure and Applied Mathematics*, 13(2):297–319, 1960.

[48] D. Ryutov, R. P. Drake, J. Kane, E. Liang, B. A. Remington, and W. M. Wood-Vasey. Similarity criteria for the laboratory simulation of supernova hydrodynamics. *The Astrophysical Journal*, 518(2):821, 1999.

[49] D. Saumon and T. Guillot. Shock compression of deuterium and the interiors of jupiter and saturn. *The Astrophysical Journal*, 609(2):1170, 2004.

[50] D.H. Sharp. An overview of rayleigh-taylor instability. *Physica D: Nonlinear Phenomena*, 12(1 - 3):3 – 18, 1984.

[51] Doug M. Smith, Stephen Cusack, Andrew W. Colman, Chris K. Folland, Glen R. Harris, and James M. Murphy. Improved surface temperature prediction for the coming decade from a global climate model. *Science*, 317(5839):796–799, 2007.

[52] Igor Sokolov. private communication, 2012.

[53] Volker Springel, Carlos S. Frenk, and Simon D. M. White. The large-scale structure of the universe. *Nature*, 440(7088):1137–1144, 04 2006.

[54] Eleuterio F. Toro. *Riemann Solvers and Numerical Methods for Fluid Dynamics - A Practical Introduction (3rd Edition)*, chapter The HLL and HLLC Riemann Solvers, pages 315–344. Springer - Verlag, 2009.

[55] Gábor Tóth, Bart van der Holst, Igor V. Sokolov, Darren L. De Zeeuw, Tamas I. Gombosi, Fang Fang, Ward B. Manchester, Xing Meng, Dalal Najib, Kenneth G. Powell, Quentin F. Stout, Alex Glocer, Ying-Juan Ma, and Merav Opher. Adaptive numerical algorithms in space weather modeling. *Journal of Computational Physics*, 231(3):870 – 903, 2012. Special Issue: Computational Plasma Physics.

[56] B. van der Holst, G. Tóth, I. V. Sokolov, K. G. Powell, J. P. Holloway, E. S. Myra, Q. Stout, M. L. Adams, J. E. Morel, S. Karni, B. Fryxell, and R. P. Drake. CRASH: A block-adaptive-mesh code for radiative shock hydrodynamics—implementation and verification. *The Astrophysical Journal Supplement Series*, 194(2):23, 2011.

[57] B. van der Holst, G. Tóth, I.V. Sokolov, B.R. Torralva, K.G. Powell, R.P. Drake, M. Klapisch, M. Busquet, B. Fryxell, and E.S. Myra. Simulating radiative shocks with the CRASH laser package. *High Energy Density Physics*, 9(1):8 – 16, 2013.

[58] Bram van Leer. Towards the ultimate conservative difference scheme. v. a second-order sequel to godunov's method. *Journal of Computational Physics*, 32(1):101 – 136, 1979.

[59] Alexander L. Velikovich. Analytic theory of richtmyer–meshkov instability for the case of reflected rarefaction wave. *Physics of Fluids*, 8(6):1666–1679, 1996.

[60] Alexander L. Velikovich and Guy Dimonte. Nonlinear perturbation theory of the incompressible richtmyer-meshkov instability. *Phys. Rev. Lett.*, 76:3112–3115, Apr 1996.

[61] N. Wygoda, E. Waxman, and DA Frail. Relativistic jet dynamics and calorimetry of gamma-ray bursts. *The Astrophysical Journal Letters*, 738:L23, 2011.

[62] Yumin Yang, Qiang Zhang, and David H. Sharp. Small amplitude theory of richtmyer–meshkov instability. *Physics of Fluids*, 6(5):1856–1873, 1994.